Efficient Gene Delivery of Tailored Amphiphilic Polypeptides by Polyplex Surfing

Paul Klemm, Jana Solomun, Marko Rodewald, Maren Kuchenbrod, Veit Hänsch, Friederike Richter, Jürgen Popp, Christian Hertweck, Stephanie Hoeppener, Colin Bonduelle, et al.

Efficient Gene Delivery of Tailored Amphiphilic Polypeptides by Polyplex Surfing

Paul Klemm,[†] Jana I. Solomun,[†] Marko Rodewald,[†] Maren T. Kuchenbrod, Veit G. Hänsch, Friederike Richter, Jürgen Popp, Christian Hertweck, Stephanie Hoeppener, Colin Bonduelle, Sébastien Lecommandoux, Anja Traeger,[*] Stephanie Schubert[*]

Laboratory of Organic and Macromolecular Chemistry (IOMC), Friedrich Schiller University Jena, Humboldtstrasse 10, 07743 Jena, Germany
P. Klemm, J. I. Solomun, M. T. Kuchenbrod, F. Richter, S. Hoeppener, A. Traeger, S. Schubert

Leibniz Institute for Photonic Technology Jena, Member of Leibniz Health Technologies, Albert-Einstein-Strasse 9, 07745 Jena, Germany
M. Rodewald, J. Popp

Institute of Physical Chemistry and Abbe Center of Photonics, Friedrich Schiller University Jena, Lessingstrasse 10, 07743 Jena, Germany
M. Rodewald, J. Popp

Department of Biomolecular Chemistry, Leibniz Institute for Natural Product Research and Infection Biology, Hans Knöll Institute, Beutenbergstrasse 11a, 07745 Jena, Germany
V. G. Hänsch, C. Hertweck

Univ. Bordeaux, CNRS, Bordeaux INP, LCPO, UMR 5629, F-33600, Pessac, France
C. Bonduelle, S. Lecommandoux

Jena Center for Soft Matter (JCSM), Friedrich Schiller University Jena, Philosophenweg 7, 07743 Jena, Germany

P. Klemm, J. I. Solomun, M. Rodewald, M. T. Kuchenbrod, F. Richter, J. Popp, S. Hoeppener, A. Traeger, S. Schubert

*Correspondence: stephanie.schubert@uni-jena.de, anja.traeger@uni-jena.de

†Paul Klemm, Jana I. Solomun and Marko Rodewald contributed equally to the study.

ABSTRACT

Within this study, an amphiphilic and potentially biodegradable polypeptide library based on poly[(4-aminobutyl)-L-glutamine-*stat*-hexyl-L-glutamine] (P(AB-L-Gln-*stat*-Hex-L-Gln)) was investigated for gene delivery. The influence of varying proportions of aliphatic and cationic side chains affecting the physicochemical properties of the polypeptides on transfection efficiency was investigated. A composition of 40 mol% Hex-L-Gln and 60 mol% AB-L-Gln (**P3**) was identified as best performer over polypeptides with higher proportions of protonatable monomers. Detailed studies of the transfection mechanism revealed strongest interaction of **P3** with cell membranes, promoting efficient endocytic cell uptake and high endosomal release. Spectrally, time-, and z-resolved fluorescence microscopy further revealed the crucial role of filopodia surfing in polyplex-cell-interaction and particle internalization in lamellipodia regions, followed by rapid particle transport into cells. This study demonstrates the great potential of polypeptides for gene delivery. Thereby, the amphiphilic character improves performance over cationic homopolypeptides, and the potential biodegradability is advantageous toward other synthetic polymeric delivery systems.

KEYWORDS: Ring opening polymerization, polypeptide, gene delivery, filopodia surfing, transfection, fluorescence microscopy

47 **TOC**

48

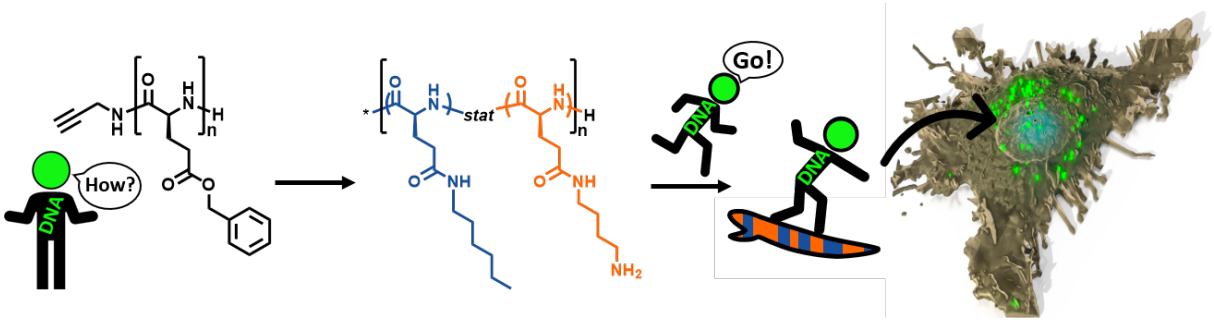

49

50

INTRODUCTION

Synthetic polypeptide-based materials are analogues to functional, *e.g.*, antimicrobial peptides[1] and a powerful tool often used in drug,[2, 3] and gene delivery[4, 5] and controlled protein release.[6] In particular, the development of suitable vectors for gene delivery, offering versatile possibilities for the treatment of diseases with genetic origin or for vaccination, has attracted increasing attention.[7, 8] To fulfill its tasks, a gene delivery vector must combine several features, *e.g.,* extracellular protection of nucleic acids from nucleases, uptake into targeted cells and sufficient release of the cargo at its site of action.[9, 10] Cellular uptake plays a crucial role in transfection, as one of the main barriers that must be overcome and being critical for the intracellular faith of the gene delivery vector and its cargo.[11, 12] To study the uptake mechanism of polyplexes, high-resolution imaging provides a powerful tool, *e.g.* to track active uptake *via* endocytosis by polyplex surfing on filopodia, which are thin membrane protrusions for scanning the cellular environment.[13]

Among non-viral gene delivery vectors, especially cationic polymers, including polypeptides, have been evaluated. One prominent example is poly(L-lysine) (PLL) as one of the first non-viral vectors, successfully complexing nucleic acids into polyplexes but revealing low transfection efficiency due to lacking endosomal escape capability.[14, 15] Besides protonation, also the secondary structure is a decisive factor for the delivery efficiency of polypeptides. As firstly observed for cell-penetrating peptides (CPP), an ordered α-helical or β-sheet[16] secondary structure promotes cell penetration and membrane interaction, while a random coil formation as observed for PLL lacks this ability.[17, 18] The interaction of CPPs with cellular membranes is further enhanced by incorporation of hydrophobic moieties along the amino acid sequence creating secondary amphipathic cationic peptides with changed charge distribution, resulting in improved cellular uptake.[19, 20] However, these short peptides often fail to sufficiently condense and bind genetic material.[21, 22] Ring opening polymerization (ROP) of amino acid *N*-carboxyanhydrides (NCA) allows to generate high molar mass compounds with tailor-made

properties and functionalities by the choice of different monomers and initiators.[5, 23, 24] Furthermore, additional post modification of polypeptides is a valuable method for further fine tuning of the materials. Click chemistry is widely used in this regard as both alkenyl and azide functions are completely inert in ROP. Therefore, various strategies for introducing clickable moieties were demonstrated, such as functional monomers[25, 26] or the use of a suitable initiator.[27] Alternatively, simple starting materials like poly(γ-benzyl-L-glutamate) (PBLG)[28, 29] or poly(L-glutamic acid) (PGA)[30, 31] can be explored for the creation of more complex structures. In this regard, post-modifications such as esterification, aminolysis and amidation are applied and allow applications of polypeptides in gene[32, 33] and drug delivery.[34] The potential of PGA has already led to a polymer-drug-conjugate, PGA-paclitaxel (CT-2103) [XYOTAX], which is currently in clinical trials for cancer therapy.[35, 36] So far, for gene delivery, mainly cationic homopolypeptides with ordered secondary structures have been investigated, showing improved efficiency compared to their random coil counterparts,[37, 38] and only few studies explored the potential of amphiphilic polypeptides in transfection.[39-41]

In this study, we now combine the beneficial properties, *i.e.*, an ordered secondary structure and a tailored cationic/hydrophobic balance, for the design of synthetic polypeptides for gene delivery. We present a small library of synthetic amphiphilic polypeptides **P1** to **P5** based on poly[(4-aminobutyl)-L-glutamine-*stat*-hexyl-L-glutamine] (P(AB-L-Gln-*stat*-Hex-L-Gln)). The amphiphilic polypeptides were prepared *via* a four-step synthetic route, characterized in terms of their physicochemical properties depending on the ratio of AB-L-Gln- and Hex-L-Gln, formulated into DNA polyplexes and screened for their gene delivery potential. Here, the amphiphilic polypeptide **P3**, which has a high proportion of hydrophobic side chains and ordered secondary structures but still remains soluble in aqueous buffers, showed the highest efficiency. To gain insight into the transfection mechanism and the influence of the cationic/hydrophobic balance on membrane interactions, endosomal release ability and cellular uptake were studied. For an even deeper understanding of the polyplex acquisition, the transport

and the internalization process by the cells, spectrally, time- and z-resolved fluorescence microscopy of live and fixed cells and complementary transmission electron microscopy were employed. Thereby, an filopodia and lamellipodia-based initial acquisition mechanism of the amphiphilic polypeptides was identified, which is followed by cellular internalization. Overall, this study highlights the importance of the cationic/hydrophobic balance of amphiphilic polypeptides for transfection efficiency and further reveals the mechanism of the so far underestimated and unstudied step of initial acquisition of amphiphilic polypeptides by lamellipodia and filopodia. These findings are thus giving essential insights for the further design of tailor-made polypeptides for efficient gene delivery.

EXPERIMENTAL

Ring opening polymerization of BLG-NCA. In a glovebox filled with argon, BLG-NCA (12 g, 45.68 mmol) was added to a fire-dried Schlenk flask and dissolved in 48 mL dimethylformamide (DMF, c_M = 0.95 M). For the initiator stock solution, 200 µL propargyl amine (3.12 mmol) were diluted in 1 mL anhydrous DMF (c = 2.60 M). The polymerization was initiated by adding 175 µL of the initiator stock solution (monomer to initiator ratio (M/I) = 100) to the highly agitated reaction solution. The solution was stirred overnight at room temperature (RT) under inert atmosphere. The conversion of the monomer was followed by infrared (IR) measurements (Figure S1). The resulting solution was precipitated in a large excess of diethyl ether. The solid was separated by centrifugation (2132 g, 4 °C, 4 min) and washed three times with 30 mL diethyl ether. All supernatants were discarded. A colorless powder was obtained by freeze-drying. Yield: 8.88 g (88 %). The polymer was characterized by proton nuclear magnetic resonance (^{1}H-NMR) spectroscopy in deuterated trifluoroacetic acid (d-TFA) including traces of deuterated chloroform ($CDCl_3$, Figure S2B), size exclusion chromatography (SEC) in dimethylacetamide (DMAc) containing 0.21 wt% LiCl (Figure S3A), IR (Figure S4) and Raman spectroscopy (Figure S5).

PGA synthesis *via* ester hydrolysis of PBLG side chains. PGA was synthesized according to a known procedure.[42] To a solution of PBLG (3 g, 15.43 mmol BLG units) in 22.5 mL TFA, 3.4 mL HBr (48 %, 62.61 mmol, 4 eq. per BLG unit) were added dropwise. The solution was stirred for 18 h at RT. The reaction mixture was precipitated in a large access of diethyl ether. The precipitant was separated by centrifugation (2132 g, 4 °C, 4 min) and washed three times with diethyl ether. All supernatants were discarded. A colorless powder was obtained by freeze-drying. Yield: 1.66 g (92 %). The product was characterized by ^{1}H-NMR spectroscopy in d-TFA including traces of $CDCl_3$ (Figure S2A), by SEC in 0.08 M Na_2HPO_4/0.05 % NaN_3 (pH = 9) solution as eluent (Figure S3B), by IR (Figure S4) and Raman spectroscopy (Figure S5), and by elemental analysis (found: Br 1.79 %).

General procedure of 1-Ethyl-3-(3-dimethylaminopropyl)carbodiimide (EDC) coupling of *n*-hexylamine (HexA) and *N*-(*tert*-butoxycarbonyl)-1,4-diaminobutylamine (BocDAB) with PGA. The detailed amounts of the reactants are summarized in Table S2. PGA was dissolved in DMF (c = 0.47 M). Successively, hydroxybenzotriazole monohydrate (HOBt, 1.5 eq. per L-Glu unit), HexA (1.10 - 0.31 eq. per L-Glu unit) and BocDAB (0.5 - 0.1 eq. per L-Glu unit) were added and the reaction mixture was stirred for 10 min. EDC (1.50 eq. per L-Glu unit) was added to the resulting suspension and stirred for 18 h at RT. The reaction mixture was precipitated in a large excess of diethyl ether. The solids were separated by centrifugation (2132 g, 4 °C, 4 min) and washed 3 times with diethyl ether. All supernatants were discarded. After drying under reduced pressure, the residue was washed three times with water. A colorless powder was obtained by freeze-drying. The product was characterized by ^{1}H-NMR spectroscopy in d-TFA including traces of $CDCl_3$ (Figure 1) and by SEC in DMAc containing 0.21 wt% LiCl (Figure S3A) as well as by IR spectroscopy (Figure S7). The respective amount of BocDAB or HexA (mol% and degree of polymerization (DP)) in each compound, summarized in Table 1, was calculated by area correlation of the characteristic signals in the

^{1}H-NMR spectra using the Peak Analyzer of Origin 9.1.0G (© by OriginLab Corporation), according to a procedure published elsewhere, Figure S8.[5] In addition, the DP of PBLG was presumed as total DP of **PP1** - **PP4** and **P5**. The theoretical molar mass ($M_{n,theo}$) was calculated by adding the molar mass of all 96 units and of the initiator.

General procedure of Boc deprotection (P1 to P4). The detailed amounts of the reactants are summarized in Table S3. In a reaction vessel, poly[(4-(N-tert-butoxycarbonylaminobutyl)-L-glutamine-*stat*-hexyl-L-glutamine] (P(BocAB-L-Gln-*stat*-Hex-L-Gln)) (250 mg) was dissolved in 2.5 mL TFA and stirred overnight at RT. Then, the pH value of the reaction solution was adjusted to 7.4 using a saturated solution of $NaHCO_3$. The resulting mixture was dialyzed against water with a regenerated cellulose membrane (MWCO 3.5 kDa, SpectraPor RC, Carl Roth) with regular water changes to remove all salt impurities. A colorless powder was obtained by freeze-drying. The product was characterized by ^{1}H-NMR spectroscopy in d-TFA including traces of $CDCl_3$ (Figure S9), Raman- (Figure S5) and CD spectroscopy (Figure 1B).

Polyplex formulation. pDNA-loaded polyplexes were formulated either in phosphate buffered saline solution (PBS) or 4-(2-hydroxyethyl)-1-piperazineethanesulfonic acid) (HEPES) buffered glucose solution (HBG, 5 % (w/v) glucose, 20 mM HEPES, pH 7.4). Therefore, stock solutions of the polypeptides in PBS or 0.2 M sodium acetate buffer (pH 5.8) were diluted with PBS (PBS polyplex) or HBG buffer (HBG polyplex), respectively. To obtain a nitrogen to phosphate (N/P) ratio of 5 and 10, the polymers were mixed with pDNA dissolved in ultrapure water at a volume ratio of 1:2 followed by vortexing for 10 s. The samples were incubated for 15 min at RT prior to usage.

Cell culture. The mouse fibroblast cell line L-929 was cultured in Dulbecco's modified eagle medium (DMEM, 1 g L^{-1} glucose), supplemented with 10 % (v/v) fetal bovine serum (FBS),

100U mL^{-1} penicillin, 100 µg mL^{-1} streptomycin (D10) at 37 °C in a humidified 5 % (v/v) CO_2 atmosphere.

Transfection of L-929 Cells. For transfection experiments, L-929 cells were seeded in a 48-well format at a density of 0.1×10^6 cells mL^{-1} in 250 µL D10 per well and incubated for 24 h. The medium was changed to 225 µL fresh D10 1 h prior to treatment. Polyplexes were prepared as described above using DH-pEGFP-N1 pDNA. pKMyc pDNA (not encoding for green fluorescent protein) was used as negative control. The polyplexes were prepared at N/P ratios of 5 and 10 and final pDNA concentrations of 3 and 4.5 µg mL^{-1} per well. The cells were treated with 25 µL of the samples or respective buffer as control and incubated with the samples for 24 h. Subsequently the cells were detached by trypsin-ethylenediaminetetraacetate (trypsin-EDTA), resuspended in Hanks' balanced salt solution (HBSS) buffer (supplemented with 2 % FBS and 20 mM HEPES) and measured *via* flow cytometry (λ_{Ex} = 488 nm combined with a 525/40 nm bandpass filter, FITC channel). Viable single cells expressing green fluorescence protein (GFP) were identified by gating to the negative control (polyplex with pKMyc pDNA). The gating strategy is shown in detail in Figure S10. Cells were further imaged by fluorescence microscopy using brightfield imaging and the FITC channel (λ_{Ex} = 469/35 nm, λ_{Em} = 525/39 nm) [43].

Endosomal escape *via* calcein release assay. For investigations of endosomal escape, a calcein assay was performed as previously described with slight adaptions of the procedure.[44, 45] L-929 cells were seeded in 24-well ibiTreat plates at a density of 0.1×10^6 cells mL^{-1} in 500 µL D10 and incubated for 24 h. The medium was changed to fresh D10 1 h prior to treatment. Polyplexes were prepared as described above (N/P 10, 4.5 µg mL^{-1} pDNA per well). For treatment, 10 µL calcein (2.5 mg mL^{-1}) were added per well to give a final concentration of 50 µg mL^{-1}, directly followed by 50 µL of the samples. Following 1 h of incubation, the cells

were washed twice with warm FC buffer and 500 µL warm D20 (DMEM supplemented with 20 % FBS) was added. The cells were subsequently stained with 8 µM Hoechst 33342 and imaged *via* confocal laser light scanning microscopy (CLSM). Calcein was excited at 488 nm by applying the argon laser (1 %) using emission filters for 490–544 nm. For excitation of Hoechst, the Argon laser at 405 nm (0.5 %) was used with a detection filter for 410–469 nm. To avoid cross talk, calcein and Hoechst were imaged in two separate tracks using the frame scan modus. Images were acquired using the ZEN software, version 2.3 SP1 (Zeiss) and were processed using ImageJ (Version 1.52a, National Institutes of Health).[46] Image analysis for quantification of cells with released calcein, was conducted as described before, with slight adjustments of image processing steps and is described in detail in the SI [45].

Cellular uptake of the polyplexes in L-929 cells measured *via* flow cytometry. To study cellular uptake *via* flow cytometry, L-929 cells were seeded in a 48-well format as described for transfection experiments. The medium was changed to 225 µL fresh D10 1 h prior to treatment. For polyplex preparation (N/P 5 and 10, 1.5 µg mL^{-1} pDNA), pKMyc pDNA was labeled with YOYO-1 iodide (0.027 nmol per 1 µg pDNA) and subsequently mixed with the polypeptides as described above. In the following, the assay was performed as described before.[44] Briefly, 25 µL of the samples were added per well and the cells were incubated with the samples for 1 h, 4 h and 24 h. Subsequently, the cells were detached and resuspended as described for transfection experiments and Trypan Blue solution was added at a concentration of 0.04 % per well. Additionally, the cells were stained once with propidium iodide (PI) to gate the viable cells. PI was added to a final concentration of 1 µg mL^{-1}, and the cells were then measured *via* flow cytometry (λ_{Ex} = 488 nm, 610/20 nm bandpass filter). PI-negative cells were gated according to the positive control linear poly(ethyleneimine) (LPEI) without pDNA, final concentration of 100 µg mL^{-1}) and negative control (PBS buffer). YOYO-1 fluorescence was measured using the FITC channel. Viable single cells showing increased YOYO-1 fluorescence

intensity (FI) were identified by gating to the negative control (pDNA labeled with YOYO-1) and the relative mean fluorescence intensity (rMFI) of all viable single cells was calculated relative to the negative control. A detailed gating strategy is shown in the SI (Figure S11).

Cellular uptake of P2 and P3 polyplexes in L-929 cells imaged by fluorescence microscopy. To monitor cellular uptake *via* fluorescence microscopy, L-929 cells were seeded into 4-well glass bottom dishes (Greiner) at a density of 0.2×10^6 cells mL^{-1} in 500 µL D10 and incubated for 24 h. Polyplexes of **P2** (N/P 5) and **P3** (N/P 10) were prepared using pKMyc pDNA, which was labeled with YOYO-1 as described above at a final pDNA concentration of 1.5 µg mL^{-1} per well. For live cell imaging, the cells were stained with CellMask™ Deep Red membrane stain (CMDR), Thermo Fisher Scientific, 1× working solution in HBSS buffer prepared from 1000x concentrated stain solution). For staining, the supernatant was removed, the cells were washed once with 500 µL PBS buffer, and 100 µL of the staining solution was added per well. After 8 min of incubation, the staining solution was removed, and the cells were washed three times with PBS buffer, followed by addition of 250 µL fresh D10 per well. For treatment, 50 µL of the polyplex solution was diluted with 200 µL D10 and added to the cells to obtain a final volume of 500 µL per well. After incubation and live cell imaging (100 min), the cells were washed three times with PBS, and cells treated with **P3** polyplex were fixed with 4 % paraformaldehyde (PFA) solution in water by 10 min incubation at 37 °C. The cells were then washed three times with PBS, 500 µL PBS was added per well and the cells were stored in the fridge overnight before z-resolved measurements. For measurements of fixed cells treated with **P2** polyplex, the medium was changed to 450 µL fresh D10 1 h prior to treatment. Subsequently, 50 µL of **P2** polyplex solution was added per well and incubated with the cells for 15 min, followed by CMDR staining and fixation with PFA as described above, and immediate transfer to the microscope.

Two-channel images (CMDR, YOYO-1) were recorded using simultaneous excitation (488 nm (YOYO-1), 650 nm (CMDR); white light laser, Leica) and the internal monochromators. For all data, except the spectrally resolved YOYO-1 data, the signals were detected in the spectral ranges 503 - 628 nm and 665 - 800 nm, respectively. For spectrally resolved YOYO-1 data, the excitation wavelength was set to 483 nm and detection was performed in increments of 5 nm and with detection windows of 5 nm. The pinhole for confocal operation was opened to account for 1 airy disk in all measurements. Detailed parameters for every measurement are part of the SI.

Sample preparation for imaging of cellular uptake of P2 and P3 polyplexes in L-929 cells by transmission electron microscopy (TEM). For uptake studies *via* TEM, L-929 cells were seeded into 6-well cell culture plates at a density of 0.5×10^6 cells mL^{-1} in 2 mL D10 and incubated for 24 h. Medium was changed to 1.8 mL fresh D10 1 h prior to treatment. Polyplexes of **P2** (N/P 5) and **P3** (N/P 10) were prepared using pKMyc pDNA at a final pDNA concentration of 4.5 µg mL^{-1} per well and 200 µL of the sample was added per well. After incubation for 1 h, the cells were detached by trypsin-EDTA and resuspended in 450 µL D10. For embedding, the cells were washed three times with PBS and centrifuged at 100 g for 2 min.[47] The cells were fixated on ice for 1 h in an 2.5 % glutaryl aldehyde, 1 % osmium tetroxide PBS solution. To remove any residues, the fixed cells were subsequently washed twice for 15 min with PBS. Dehydration of the cells was reached by replacing the buffer solution stepwise (50 %, 70 %, 90 %, 100 %) with ethanol (EtOH). 18 µL 2,4,6-tri(dimethylaminomethyl) phenol solution (DMP-30) were added per mL to a previously prepared Embed812 (EMbed 812, dodecenyl succinic anhydride (DDSA) and methyl-5-norbornene-2,3-dicarboxylic anhydride (NMA) in the ratio 1:1.1:0.25) solution. In a first step, the embedding solution was added to the cells for 1 h with a ratio of 2:1 with EtOH. Subsequently, the cells were centrifuged at 100 g for 8 min and the residual embedding solution

was removed followed by adding pure Embed812/DMP-30 solution, incubation at RT overnight and centrifugation again. After the removal of the residual embedding solution, freshly prepared Embed812/DMP-30 solution was added and incubated for 2 h at RT. Afterwards the cells were transferred to BEEM® capsules and centrifuged again. Residual embedding solution was removed before fresh Embed812/DMP-30 solution was added, and the samples were dried at 60 °C overnight in the drying oven. The dried sample was cut in 100 nm slices. Each slice was stained with 4 % uranyl acetate solution for 20 min and subsequently with lead citrate for 5 min. The slices were transferred onto Quantifoil® carbon supported film grids (Cu 300 mesh) and subjected to TEM measurements. For cryo-TEM investigations, 9 µL of the particle solutions were deposited on a Quantifoil grid (R2/2) in a Vitrobot Mark IV. Samples were blotted at a blot force of -1 for 1 s and rapidly immersed into liquid ethane serving as the cryogen. Grids were transferred into the cryo-holder (Gatan 626) utilizing the Gatan cryo transfer stage. During the entire process after vitrification in ethane, the temperature was maintained at temperatures lower than 175 °C. Images were acquired on a side-entry CCD camera (MegaView, Olympus Soft Imaging Solutions).

Statistical analysis. Statistically significant differences within transfection and uptake experiments measured by flow cytometry were determined by analyzing multiple groups by two-way mixed analysis of variance (two-way mixed ANOVA) and a Bonferroni's post-hoc test. Statistical significance is indicated as follows: */# $p < 0.05$, **/## $p < 0.01$, and ***/### $p < 0.001$ and analysis was conducted using OriginPro2021 software.

RESULTS AND DISCUSSION

Polymer synthesis and characterization. Cationic functionalities are necessary to enable the complexation of pDNA and the formation of a polyplex. Therefore, a small library consisting of the pure polycation P(AB-L-Gln) P1, the amphiphilic polypeptides P(AB-L-Gln-*stat*-Hex-L-

Gln) P2 - P4 and the hydrophobic P(Hex-L-Gln) P5 were prepared at room temperature (RT) by amidation of PGA and deprotection of the Boc-AB-L-Gln units of the protected polymers (PP1 - PP4), Scheme 1. PGA was obtained by classical ester hydrolysis of the starting material PBLG [42].

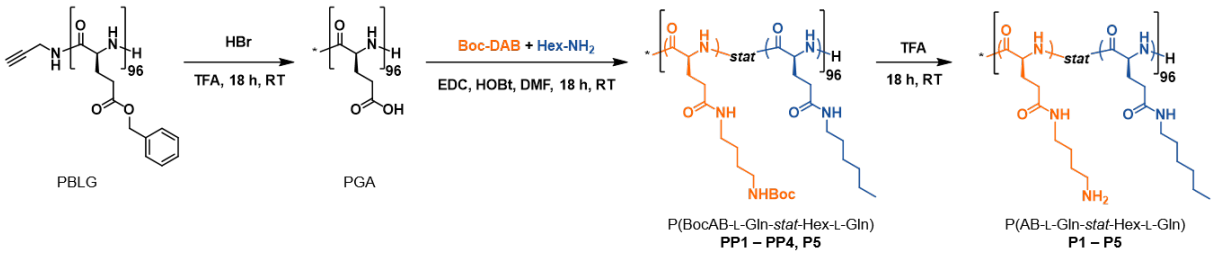

Scheme 1: Schematic representation of the synthesis route of P(AB-L-Gln-*stat*-Hex-L-Gln) **P1** (100 mol% AB-L-Gln : 0 mol% Hex-L-Gln), **P2** (84 mol% : 16 mol%), **P3** (60 mol% : 40 mol%), **P4** (30 mol% : 70 mol%) and **P5** (0 mol% : 100 mol%).

PBLG was synthesized *via* ROP from BLG-NCA. Propargyl amine was used as an initiator with a M/I of 100 to allow a simplified determination of the DP based on the isolated signal in the ^{1}H-NMR of the methylene protons at $\delta = 4.07$ ppm (Figure S2). The conversion of the monomer was monitored by IR spectroscopy. After four days, the complete disappearance of the characteristic NCA bands at $\tilde{\nu} = 1853$ cm^{-1} and 1786 cm^{-1} indicated complete conversion (Figure S1). PBLG is narrowly distributed with a polydispersity index ($Đ$) of 1.07 as determined by SEC (Figure S3, Table S1). Using the ^{1}H-NMR spectrum in Figure S2, a chain length of on average 96 monomer units was obtained by integrating the signal from the chiral proton in the polymer backbone at $\delta = 4.76$ ppm, relative to the two protons of the methylene group of the starting group at $\delta = 4.07$ ppm. Starting from PBLG, three modification steps were required to reach the targeted structures **P1** to **P4** (Scheme 1).

The cleavage of the benzyl ester of PBLG led to PGA. The Raman spectra of both compounds (Figure S5) show the complete disappearance of the aromatic CH stretching vibration at $\tilde{\nu} = 3065$ cm^{-1}, as well as the aromatic ring breathing mode at $\tilde{\nu} = 1004$ cm^{-1} and the accompanying peak at $\tilde{\nu} = 1031$ cm^{-1}, which is typical for mono-substituted aromatic compounds and, thus, indicates complete conversion. Accordingly, IR spectra of PGA (Figure

S4) show the presence of carboxylic OH groups at $\tilde{\nu} \sim 1700\ cm^{-1}$ and the signal at $\tilde{\nu} \sim 3300\ cm^{-1}$, which is partially obstructed by the broad NH stretching mode. The disappearance of all benzylic protons in the ^{1}H-NMR spectra (Figure S2) further confirms the successful hydrolysis of the ester side arms. Elemental analysis of PGA showed 1.79 % Br, indicating the presence of some hydrobromides and potentially a partial HBr addition to the triple bond. However, stoichiometric conversion with 2 eq. HBr could only account for 1.26 % Br, and all intermediates (**PP1 - PP4**) and final products (**P1 - P5**) show the characteristic resonance of C≡C triple bonds at 2130 cm^{-1} in their Raman spectra (Figure S5), indicating that addition of HBr in the first reaction step is a minor concern. Because of the lack of suitable, *i.e.*, non-overlapping and constant peaks in ^{1}H-NMR, quantitative statements about the DP of PGA are difficult to make. SEC measurements of PGA (Figure S3B) show a tailing that can be explained by interactions with the column. The high molar mass (M_n) and $Đ$ of PGA compared to PBLG as determined by SEC can be explained by the aqueous eluent and a different calibration (Table S1).

After ester hydrolysis, the carboxylic acid functionalities were now available to couple amines in various ratios by activation with EDC and HOBt activation. Therefore, the mono-protected compound of DAB, *i.e.,* BocDAB, was used to prevent crosslinking when working with dual-functional DAB. In addition, hydrophobic HexA was chosen to lower the toxicity of the polycation while ensuring efficient complexation of pDNA and preventing random coil formation as secondary structures. To investigate the changes in chemical, structural, spectroscopic, and biological behaviors, two homopolymers (**PP1** and **P5**) and three copolymers (**PP2** - **PP4**) with different ratios of HexA and BocDAB were synthesized, Table S2. **PP2** and **PP3** were synthesized with an excess of BocDAB compared to HexA, while a substoichiometric amount of BocDAB was used for **PP4**. Figure 1 shows the ^{1}H-NMR spectra of **PP1** to **PP4** and **P5**. The detection of the starting group is shown in Figure S12.

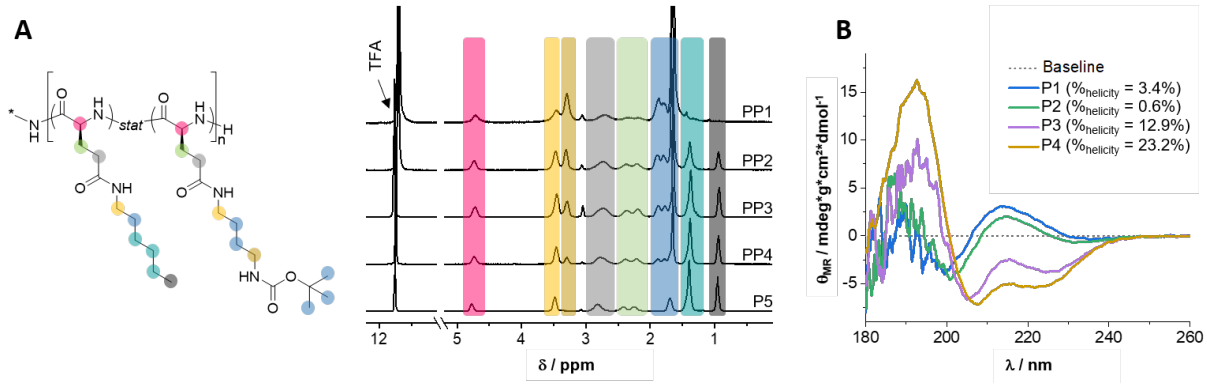

Figure 1 **A** ^{1}H-NMR spectra of **PP1** to **PP4** and **P5** measured at 25 °C and 300 MHz in deuterated d-TFA containing traces of $CDCl_3$. **B** Overlay circular dichroism (CD) spectra of **P1** – **P4** measured in 1,1,1,3,3,3-hexafluoro-2-propanol (HFiP) (c_{Pi} = 0.50 mg mL^{-1}). Mean residual ellipticity θ_{MR} calculated with Equation S6 including $\%_{helicity}$ calculated with Equation S7.

Both, ester hydrolysis and EDC coupling do not change the total DP of 96, which was determined for PBLG and, thus, also applies to the intermediates. The content of BocDAB and HexA can be determined by correlating the characteristic signals of both moieties in their ^{1}H-NMR spectrum.[5] ^{1}H-NMR studies revealed the following ratios of BocAB-L-Gln and Hex-L-Gln: **PP1** 100 mol%:0 mol%, **PP2** 84 mol%:16 mol%, **PP3** 60 mol%:40 mol%, **PP4** 30 mol%:70 mol% and **P5** 0 mol%:100 mol%, Table 1. The elugrams of **PP1** to **PP4** measured by SEC showed monomodal distributions in all cases with low *Đ* around 1.17 **(**Figure S3A). **P5** is insoluble in all common solvents except TFA, consequently, investigation with the given SEC systems was not possible. The M_n values determined by universal PS calibration are comparable to $M_{n,theo}$ calculated from the ^{1}H-NMR results, Table 1. The cleavage of the Boc protecting group from **PP1** to **PP4** in pure TFA resulted in **P1** to **P4**. The disappearance of the prominent singlet at δ = 1.6 ppm in ^{1}H-NMR spectroscopy (Figure S9A) indicates a complete deprotection of the amines of **PP1** to **PP4**. The SEC studies in Figure S9B show that polymers **P1**, **P2** and **P3** are still intact. However, in the case of **P3**, a second population elutes with a lower elution volume, indicating a higher molar mass species. This could be caused by interactions of the polymer with the stationary phase of column material or by self-assembly of

the polymer in the eluent. SEC analysis was not possible for **P4** and **P5** due to their insolubility in the eluent used.

Table 1: Results of analytical investigations of **PP1** to **PP4** and **P5**.

	^{1}H-NMR[a)]					SEC[b)]		Yield	ID
	$M_{n,theo}$	mol%$_{BocAB}$	DP	mol%$_{Hex}$	DP	M_n	$Đ$		deprot.
	kg mol^{-1}					kg mol^{-1}		%	
PP1	28.8	100	96	-	-	24.0	1.15	62	**P1**
PP2	27.5	84	81	16	15	24.7	1.13	51	**P2**
PP3	25.5	60	58	40	38	23.0	1.17	71	**P3**
PP4	22.9	30	29	70	67	21.5	1.21	68	**P4**
P5	20.4	-	-	100	96	-	-	69	**P5**

a) ^{1}H-NMR measured in d-TFA containing traces of $CDCl_3$ at 25 °C and 300 MHz. In each case, sum of DP_BocAB and DP_Hex gives a total DP of 96 (DP of PBLG). b) SEC measurements were determined by using DMAc/0.21 wt% LiCl as eluent, RI detector and a polystyrene (PS) calibration.

Investigation of the secondary structures. Previous studies have already shown that the secondary structure of a polypeptide has an impact on effective cell uptake through destabilization of the membrane.[48] In Figure S13A, IR spectra of solid **P1** to **P5** show the influence of the aliphatic side arms. With increasing content of HexA, the band of β-sheets also increased at $\tilde{\nu}_\beta \sim 1625$ cm^{-1}, while the band for α-helices decreases at $\tilde{\nu}_\alpha \sim 1645$ cm^{-1}. In addition, it can be suspected that less amount of random coil structures was formed ($\tilde{\nu}_{rc} \sim 1650$ cm^{-1} and $\tilde{\nu}_{rc} \sim 1538$ cm^{-1}) with an increasing content of HexA. Therefore, in solid state, it can be assumed that at the transition from **P2** to **P4** the content of α-helices and β-sheets exceeds that of random coil formation. Merely the spectra of **P1** complicates the interpretation of the macrostructure of the compound. However, the shape of the curve may indicate overlapping bands of α-helices, β-sheets, and random coil formations. Therefore, it can be assumed that **P1** has the highest content of random coil formation compared to the other

compounds probably due to its purely cationic structure. To confirm the results of the solid-state IR studies, CD measurements were performed on polymers **P1** to **P4** dissolved in HFiP, a solvent suitable for CD spectroscopy.[49] The curves of **P1** and **P2** show the characteristic shape of coil formation with a maximum at 215 nm (Figure 1B).[50] In contrast, polymers **P3** and **P4** show two minima at 205 and 222 nm, which can be assigned to α-helix formation. In addition, CD measurements were performed with polyplexes of **P1** to **P3** dissolved in phosphate buffered saline (PBS, pH 7.4) (N/P 10), Figure S13B. Due to their insolubility, **P4** and **P5** were not suitable for polyplex formulation. The results derived from the profiles of **P1**, **P2** and **P3** in physiological environment are comparable to their behavior dissolved in HFiP. The spectra of the polyplexes of **P1** indicate mainly random coil formation, whereas the shape of **P2** reveals a mixture of random coil and α-helix formation.[51] The curve of the polyplexes of **P3** suggest a mixture of β-sheet and α-helix formation.

DNA binding and release. To utilize the synthesized polypeptides as gene delivery vectors, their pDNA binding and release capability was evaluated. First, the polypeptides were dissolved in PBS (pH 7.4) or acetate buffer (0.2 M, pH 5.8) to test their solubility. **P1** and **P2** were highly soluble in both buffers, while **P3** showed lower solubility in PBS. **P4** with the highest content of hydrophobic HexA groups was not soluble in both buffers and was, therefore, excluded from the study. pDNA binding was measured using the ethidium bromide binding assay (EBA). Therefore, polyplexes were prepared with ethidium bromide (EtBr) labelled pDNA in PBS (PBS polyplex) or a mixture of acetate buffer and HBG buffer (HBG polyplex) at various N/P ratios (1 to 30), followed by monitoring of EtBr fluorescence (Figure S14A). All investigated polypeptides showed pDNA binding at N/P > 1 independent of the buffer system used, as indicated by the plateau reached in relative fluorescence intensity (rFI). These results clearly show that for all polymers the N/P ratio and thus the total amount of primary amino groups (AB-L-Gln) is the decisive factor for pDNA condensation, independent of the molar ratio of

AB-L-Gln and hydrophobic Hex-L-Gln within the statistical polymers. Differences were observed in the level of the plateaus, with rFI decreasing to ~ 50 % for PBS and ~ 10 % for HBG polyplexes, indicating a stronger binding in HBG. In comparison, PBS polyplexes might be less charged either due to higher pH values or shielding of amine groups by phosphate ions present in the solution. Nevertheless, in both buffer formulations all polypeptides (**P1** - **P3**) successfully bind pDNA at N/P ratios ≥ 5. As pDNA further needs to be released within the cell for successful gene delivery, dissociation of the polyplexes in the presence of heparin as competing anion was studied by monitoring EtBr fluorescence upon addition of increasing amounts of heparin (Figure S14B). All polyplexes showed pDNA release at heparin concentrations above 9 U mL^{-1}. HBG polyplexes of all polypeptides completely released pDNA at 20 U mL^{-1}. Release efficiencies in PBS showed the same tendencies but did not reach 100 % release in all cases. These results further support the assumption of pronounced hydrophobic interactions in PBS, being less prone to displacement by highly negatively charged heparin.[52, 53] Overall, the polypeptides **P1** to **P3** showed good pDNA binding and release and are therefore suitable candidates for gene delivery.

Toxicity and transfection efficiency in L-929 cells. A PrestoBlue™ assay was performed in L-929 cells by incubating the cells with the polymers dissolved in PBS or acetate/HBG buffer to evaluate their toxicity (Figure 2A). The L-929 cell line was chosen as standard cell line for cytotoxicity testing recommended by the ISO 10993-5 guideline. Further, this cell line has been intensively investigated with regards to its uptake mechanism and intracellular trafficking of nanoparticles and polyplexes, rendering it an optimal system for the evaluation of novel gene delivery systems and their transfection mechanism.[54, 55] Substantial influence of the utilized buffer system was observed. The cytotoxicity of **P1** is least influenced by the buffer ($IC_{50, PBS}$ = 41.9 µg mL^{-1}, $IC_{50, HBG}$ = 33.6 µg mL^{-1}) followed by **P2** ($IC_{50, PBS}$ = 36.5 µg mL^{-1}; $IC_{50, HBG}$ = 18.8 µg mL^{-1}). In comparison, **P3** is substantially less toxic in PBS buffer, revealing the highest cell viability there ($IC_{50, PBS}$ = 65.1 µg mL^{-1}, $IC_{50, HBG}$ = 13.6 µg mL^{-1}) and showing

454 substantially lower toxicity than LPEI at similar concentrations. This could be attributed to a
455 higher charge density of **P3** in acetate/HBG buffer in combination with an increased proportion
456 of hydrophobic moieties leading to enhanced association with cellular membranes and thus to
457 cytotoxic effects.[56-58] In contrast, it is assumed, that hydrophobic and cationic moieties are
458 balanced in PBS buffer and excess cationic charges are shielded by the presence of phosphate
459 ions leading to improved cytocompatibility.[59] To identify suitable conditions for evaluating the
460 influence of the polymer structure on transfection efficiency L-929 cells were incubated with
461 PBS or HBG polyplexes at various N/P ratios (2, 5, 10 and 20), pDNA concentrations (1.5, 3
462 and 4.5 µg mL^{-1}) and incubation times (4 + 20 h, 24 h and 24 + 24 h) (data not shown).
463 Considering these pretests, PBS and HBG polyplexes at N/P 5 and 10 and a pDNA
464 concentration of 4.5 µg mL^{-1} were selected for the further study and incubated with L-929 cells
465 for 24 h, followed by further 24 h of incubation with fresh growth medium (24 + 24 h).
466 Transfection efficiency was measured *via* flow cytometry as percentage of viable cells
467 expressing EGFP (Figure 2B, S10, S15) and confirmed by fluorescence microscopy (Figure
468 S16, S17). Cell viability was monitored by the sideward and forward scattering (FSC/SSC) of
469 the cells (Figure S10).[44] In addition, cytotoxicity of polyplexes was evaluated *vi*a the
470 PrestoBlue™ assay after 24 h of incubation (Figure S18). The cells showed high viability
471 (> 85 % viable cells during transfection experiments (24 h + 24 h)). However, polyplexes
472 prepared in HBG caused higher cytotoxicity in comparison to PBS polyplexes, whereas at the
473 tested concentrations and N/P ratios no significant difference in transfection efficiency was
474 observed. The highest percentage of transfected cells was reached with **P3** at N/P 10 in both
475 buffers (20.7 % in PBS and 17.8 % in HBG), clearly outperforming **P1** and **P2** as well as the
476 commercial control LPEI at the same conditions (12.7 % in PBS and 12.3 % in HBG). **P1**
477 showed almost no transfection in PBS and HBG (N/P 10) (0.3 % and 1.0 % respectively),
478 whereas **P2** resulted in 2.9 % in PBS and 3.7 % in HBG (N/P 10).Among the polypeptides, **P3**
479 further resulted in the highest mean fluorescence intensity (MFI) (Figure S19) also visible by

fluorescence microscopy (Figure S16, S17). In contrast, hydrophobic cationic polypeptide systems previously investigated by our group showed much lower transfection efficiency compared to the commercial control LPEI.[5] Thus, the best performing **P3** polypeptide in this study is a promising candidate for gene delivery not only because of its simpler synthesis and higher synthetic variability, but also due to its substantially better performance in comparison to LPEI.

To get a deeper understanding of the transfection mechanism of the polypeptides, the following investigations were performed Since PBS polyplexes caused lower cytotoxicity in comparison to HBG polyplexes, without any substantial difference in transfection efficiency, the experiments were conducted exclusively with PBS polyplexes.

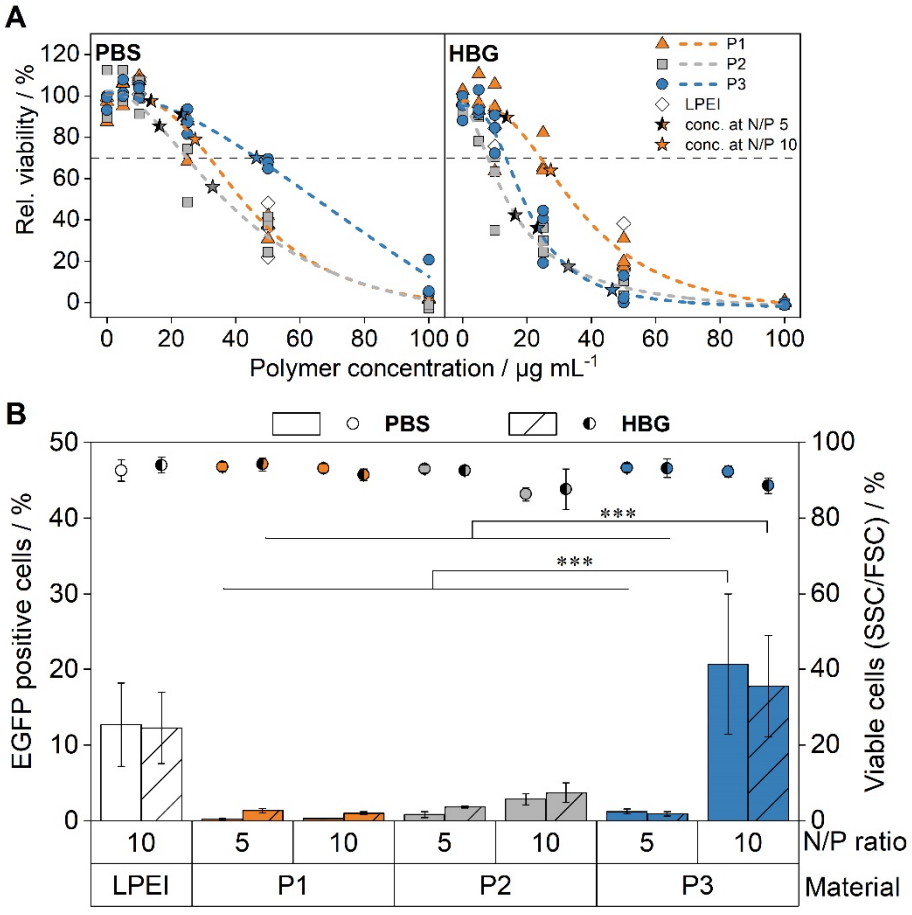

Figure 2 Evaluation of cytotoxicity and transfection efficiency in L-929 cells. **A** Cytotoxicity of **P1**, **P2** and **P3** without pDNA in the respective buffer was measured by the PrestoBlue™

assay following incubation of the cells (with the polymer) for 24 h. The dashed line indicates 70 % cell viability and stars mark the polymer concentration required in the transfection studies for the respective N/P ratio at a pDNA concentration of 4.5 µg mL^{-1} ($n \geq 3$). **B** Transfection efficiency (EGFP expression) was investigated *via* flow cytometry after 24 h incubation with the polyplexes (N/P 5 and 10, 4.5 µg mL^{-1} pDNA) followed by incubation with fresh growth medium for further 24 h (24 h + 24 h). Transfection efficiency is displayed as percentage of transfected cells in comparison to the control (polyplex with pKMyc pDNA) (mean ± SD, $n \geq 3$). Statistically significant differences between the polypeptides in the respective buffer are denoted as follows: *$p < 0.05$, **$p < 0.01$, and ***$p < 0.001$.

Transfection mechanism in L-929 cells. *Membrane Interactions and Endosomal Escape.* Membrane interactions and endosomal escape are well-known obstacles for non-viral gene delivery and were studied by a hemolysis/aggregation and a calcein release assay. Erythrocytes were incubated with PBS polyplexes at N/P 10 at various pDNA concentrations and pH values to study membrane interactions at physiological (pH 7.4) and endosomal (pH 6) conditions.[60] Then, hemoglobin release was measured as indicator for membrane disruption (Figure 3A). Additionally, erythrocyte aggregation was monitored, likewise an indicator for polymer-membrane interactions (Figure 3B). An ascending hemolytic trend was observed at both pH values, with **P3** showing the strongest hemolytic activity especially at high concentrations (11.9 ± 2.1 %). An opposing trend emerged for aggregation, with **P1** resulting in slight aggregation at high concentrations (1.03 at pH 7.4 and 1.06 at pH 6), whereas **P2** and **P3** did not show any effect (aggregation < 1.0). This proposes a different mechanism of membrane interaction for **P1**, showing merely membrane association, whereas **P2** and **P3** clearly lead to membrane leakage events. This can be attributed to the increasing proportion of HexA groups in **P2** and **P3** promoting additional hydrophobic membrane interactions, whereas the cationic homopolymer **P1** mainly interacts electrostatically.[57, 61] The formation of ordered secondary structures might also contribute to the hemolytic activity of **P3** at both physiological and endosomal pH values.[19, 59] These results point towards a high cellular uptake as well as efficient endosomal escape of **P3**, which could explain its good transfection performance.

To study endosomal release, a calcein release assay was performed. The cells were incubated simultaneously with the membrane impermeable dye calcein and the polyplexes at N/P 10 for 1 h and subsequently imaged *via* CLSM (Figure 3C, Figure S20). Endosomal release indicated by homogeneous fluorescence of calcein within the cytosol was observed for all polypeptides, with **P3** showing the highest percentage of calcein releasing cells (8.2 ± 3.1 %, Figure S21), which is in accordance with the hemolytic activity at pH 6 (Figure 3A). However, differences within the polypeptides were rather small (4.9 ± 2 % for **P1** and 5.7 ± 3.8 % for **P2**). This indicates that the endosomal release efficiency may not be the main factor contributing to the superior transfection efficiency of **P3.**

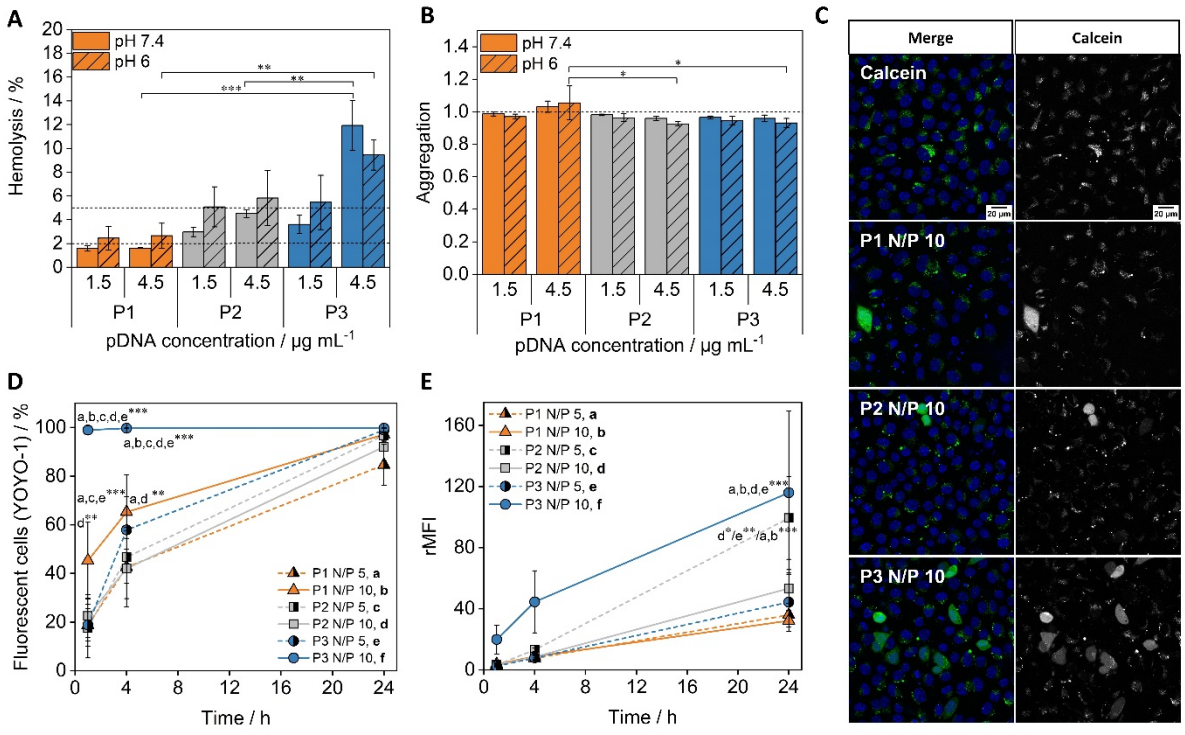

Figure 3 Investigation of the gene delivery process in L-929 cells. **A** Hemolytic activity was measured as release of hemoglobin from sheep erythrocytes after incubation with the polyplexes (N/P 10, 1.5 and 4.5 mg mL^{-1} pDNA). Erythrocytes were incubated with the polyplexes at pH 7.4 and 6 to mimic conditions present in the blood and the endosomes, respectively (mean ± SD, n = 3). **B** Aggregation of erythrocytes incubated with the polyplexes was measured as light absorption of erythrocytes. 10 kDa branched poly(ethylenimine) was used as positive control and PBS as negative control (mean ± SD, n =3). Statistically significant differences at the respective concentration and pH value are denoted as follows: *$p < 0.05$, **$p < 0.01$, and ***$p < 0.001$. **C** Representative images of the endosomal escape of polyplexes analyzed *via* CLSM are shown. Cells were incubated simultaneously with the polyplexes (N/P 10, 4.5 µg mL^{-1} pDNA) and the non-permeable dye calcein (green) for 1 h. After incubation, the cells were washed twice, and nuclei were further stained with Hoechst (blue). **D** + **E** Time-dependent uptake of polyplexes formulated in PBS was measured *via* flow

cytometry. L-929 cells were incubated with polyplexes (N/P 5 and 10, 1.5 µg mL^{-1} pDNA) for 1, 4 or 24 h. Cellular uptake is plotted as **D** percent of cells showing increased fluorescence compared to the control (YOYO-1 stained pDNA) and **E** relative mean fluorescence intensity (rMFI) of viable single cells, calculated relative to the control (YOYO-1 stained pDNA) (mean ± SD, n = 3). Statistically significant differences at the respective timepoints are indicated as follows: *$p < 0.05$, **$p < 0.01$, and ***$p < 0.001$.

Cellular Uptake via Flow Cytometry. To study cellular uptake in a time-dependent manner, L-929 cells were incubated with YOYO-1 labeled polyplexes up to 24 h. The percentage of cells with increased YOYO-1 fluorescence (YOYO-1 positive cells) and the rMFI were measured quantitatively *via* flow cytometry (Figure 3D, E, S22). Cellular uptake of all polymers is time-dependent and reached > 90 % YOYO-1 positive cells after 24 h, whereas **P3** (N/P 10) polyplexes required only 1 h for this (99.8 % YOYO-1 positive cells). The highest rMFI values were found for **P2** N/P 5 and **P3** N/P 10 polyplexes after 24 h (99.4 and 116.0 respectively), hence these were later examined in greater detail. The lowest rMFI was observed for **P1** even after 24 h (35.9 at N/P5 and 32.2 at N/P 10), which is in accordance with its low transfection efficiency. Investigation of uptake patterns measured *via* flow cytometry further underline the differences within the used polypeptides (Figure S22). While the population of YOYO-1 positive cells homogeneously shifts to higher FI values for **P3** N/P 10 polyplexes over time, only partial and broader shifts are observed for **P1** and **P2**. This indicates a homogeneous uptake of **P3** N/P 10 polyplexes, complementing the transfection results with a high number of transfected cells with high rMFI.

As the polyplex size is a crucial parameter influencing cellular uptake, dynamic light scattering (DLS) measurements were conducted (Figure S23, Table S4). **P3** N/P 10 polyplexes had a diameter (z-average) of 140 nm and a PDI of 0.16, while all other polypeptides and **P3** N/P 5 showed diameters > 1000 nm, a PDI of > 0.38 and inappropriate correlation coefficients (Figure S23), indicating the formation of larger aggregates within the samples, which might be overestimated in DLS measurements and, thus, rendering this characterization method

unsuitable for these samples. Therefore, more detailed size measurements of selected samples were performed, employing nanoparticle tracking analysis (NTA) and imaging methods including cryogenic transmission electron microscopy (cryo-TEM), fluorescence microscopy (*chapter 3.5.3.*), and TEM measurements after incubation with cells (*chapter 3.5.4*), all identifying nano-sized particles as well. Nanoparticle tracking analysis (NTA) measurements were conducted for **P3** N/P 10 and **P2** N/P 5, both showing the highest uptake in L-929 cells (Figure S24, Table S5), with measurements of **P3** N/P 10 complementing the DLS results with a mean diameter of 196 nm. Aggregate formation for **P2** N/P 5 was confirmed, however after separation of the aggregates by centrifugation, nanostructures with a mean diameter of 258 nm were measured, which were not detectable by DLS in the presence of aggregates. For potential *in vivo* applications, such aggregates can be separated by additional processing steps, *e.g.* by centrifugation or filtration. These differences in polyplex sizes and aggregation behavior may explain the differences in uptake levels in particular at shorter incubation times as particle sizes below 200 nm are promoting controlled cellular uptake by endocytosis, while aggregation results in lower or at least slower and less controlled uptake by cells.[62] This might influence transfection efficiencies, with **P3** N/P 10 polyplexes being taken up in a controlled and homogeneous manner, whereas only the nanosized portion of **P2** N/P 5 structures shows controlled uptake, and the portion of large aggregates present in the sample is either not taken up within short time periods or only occasionally by few cells.[63] Cryo-TEM measurements of **P3** N/P 10 polyplexes showed nanostructures in the size range of approx. ≤ 100 nm in diameter with slight aggregation (Figure S25). This size range is slightly smaller than intensity-weighted diameters within DLS measurements but is complementing the number-weighted diameters. The polyplexes appeared as particles with an uneven boundary, thus representing a structure and morphology in between classical polymer nanoparticle and hydrophilic polyplexes.[64, 65] The observation of such structures is in line with a previous study of us exploring amphiphilic methacrylates for gene delivery.[66] Besides particle size and morphology, the surface charge

601 plays a crucial role in cellular uptake and transfection efficiency.[67, 68] Therefore, zeta potential
602 measurement of polyplexes were conducted (Table S4). The polyplexes had a similar positive
603 zeta potential independent of the N/P ratio and polymer (+ 21.2 to 22.8 mV). It is thus assumed
604 that the surface charge is no decisive factor for the cellular uptake of the polyplexes within this
605 study.
606
607 *Details of Cellular Uptake Visualized by Fluorescence Microscopy.* To analyze the uptake
608 mechanism in more detail, the most promising polyplexes, **P2** N/P 5 and **P3** N/P 10, were
609 further investigated in L-929 cells using fluorescence microscopy. For this purpose, polyplexes
610 labeled with intercalated YOYO-1, in conjunction with cell membrane staining by CMDR,
611 were used. The dyes are spectrally fully separated with regard to both their excitation and
612 emission, enabling simultaneous imaging. No qualitative differences regarding polyplex uptake
613 and distribution could be detected after incubation with **P3** or **P2** polyplexes in a series of z-
614 resolved (Video S1, Figure 4, S26-30) and time-resolved measurements of L-929 cells (Videos
615 S2-S4, Figure S31-40). Thereby, Video S4 shows a **P3** polyplex settling to the substrate surface,
616 being subsequently 'found' by a lamellipodium and transported to the cell, before being
617 encapsulated and endocytically taken up (marked by a white arrow), representing an interesting
618 observation of the initial interaction of the polyplexes with the cells. A detailed discussion of
619 this interaction and approaching of the polyplexes to the cell surface together with their uptake
620 dynamics is provided below. Interestingly, fixated **P3**-incubated cells, which were stored in the
621 fridge overnight after fixation showed signs of polyplex disintegration as evidenced by diffuse
622 fluorescence from several locations, predominantly in areas of former hotspots of polyplex
623 uptake (Figure S28). Contrastingly, polyplexes in the main cell body seemed to be unaffected
624 (Figure S27). As already mentioned, we did not observe qualitative differences in the uptake
625 behavior and also the initial interaction of the cells with the polyplexes in time- and z-resolved
626 measurements between **P2** and **P3** polyplexes, but a slight focus drift in the time-resolved **P3**

627 measurements limited their analysis and, hence, a more detailed discussion of the **P2**
628 measurements is given in the following.
629 High resolution overview images of fixated, **P2**-incubated cells in the bottom-most layer, *i.e.,*
630 the glass-cell interface, and 2.4 µm above were recorded (Figure S41-S43). These illustrate the
631 cell structures and organization, particularly the dense network of filopodia emerging from each
632 cell and interconnecting it with its neighboring cells (Figure S41). In the YOYO-1 channel
633 (Figure S42, 43), bright dots with an apparent size (full width at half maximum of point spread
634 function $(FWHM)_{PSF,xy}$(488 nm, 1AU, 1.4 NA) ≈ 178 nm) of approximately 250 nm to 400 nm
635 located in the cytoplasm of some, but not all, cells indicate that uptake took place (0–12 dots
636 per cell, avg.: 2.4, n = 26). These observations complement the NTA measurements of
637 centrifuged **P2** polyplexes confirming the presence of nanoparticles of approx. 300 nm in
638 diameter besides larger aggregates (Figure S24 Table S5). However, due to the small particle
639 size in combination with a relatively high z-resolution, these data do not allow for reliable
640 quantitative statements about the number of dots (meaning polyplexes) per cell, because that
641 would depend strongly on the imaged plane. For individual cells and small groups of cells this
642 can be circumvented by z-resolved measurements. Figure 4A and Video S1 provide an example
643 of this approach. While in any given plane in this cell, the maximum number of bright dots we
644 were able to observe was 12, a 3D reconstruction (Figure 4E) revealed a total of 77 bright dots
645 that are scattered mostly around the nucleus. Additionally, a multitude of filopodia and intricate
646 intracellular features are visible, contextualizing the positional information (Figure 4B). The
647 time requirements for this procedure, however, are prohibitive for studying larger numbers of
648 cells, and this microscopic approach, therefore, requires statistically more powerful techniques
649 like the above discussed flow cytometry to complement it. To confirm the observed particles'
650 identification as YOYO-1 containing polyplexes, spectrally resolved measurements (Figure 4C,
651 4D) were taken in the plane indicated in Figure 4A. The combined emission spectra of all
652 11 dots closely resembles the fluorescence spectrum of DNA-intercalated YOYO-1,[69]

confirming the identification of these dots as polyplexes. Slight deviations at about 570 nm may be due to free YOYO-1. Noteworthily, for some of the more intense and thus less noisy dots, it is possible to obtain meaningful spectra of individual polyplexes, as exemplified in Figure 4D.

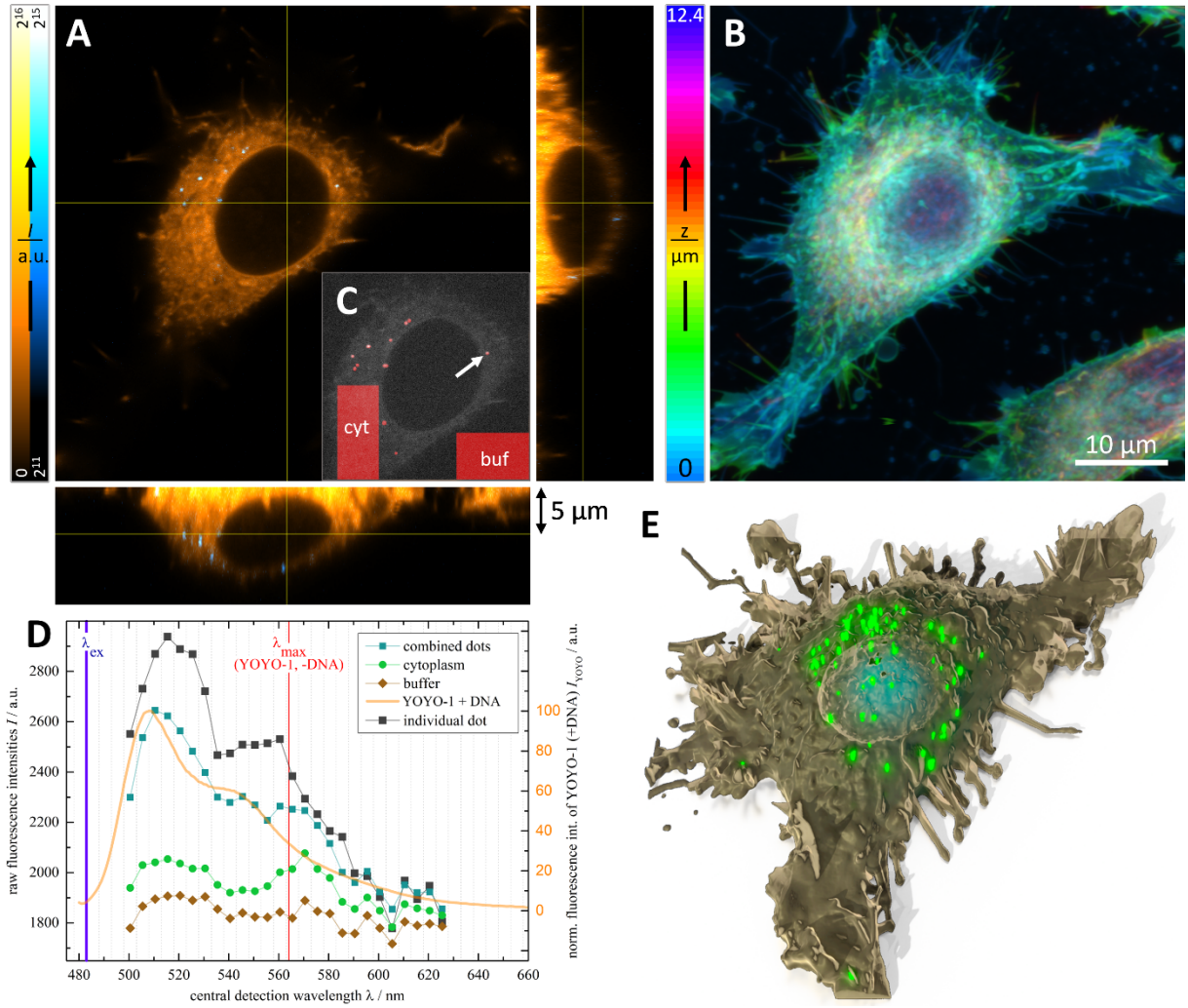

Figure 4 z-Resolved and λ-resolved fluorescence microscopy images of L-929 cells after incubation with **P2** N/P 5 polyplexes (15 min) and PFA fixation. **A** z-Stack with orthogonal views at positions indicated by yellow lines. The central image depicts the plane 5 µm above the microscope slide in which the subsequent λ-scan was performed. Orange: CMDR fluorescence, blue-cyan: YOYO-1 fluorescence indicating polyplexes. Intensities are scaled linearly along the indicated color bars. **B** Maximum intensity projection (MIP) of the CMDR channel of the same z-stack after intensity adjustment ($I_{new} = (1 + 0.075z)I_{old}$ with $z = 0…62$ being the slice number) and color coding along the z-axis. **C** MIP along the λ–axis of an emission scan ($\lambda_{ex} = 483$ nm, $\Delta\lambda_{det} = 5$ nm). Eleven polyplexes were manually identified (red overlay). **D** Emission spectra of cytoplasm, PBS, and polyplexes, averaged over all respectively labeled pixels in **C**, alongside an individual polyplex (marked by white arrow in) spectrum and a reference spectrum of YOYO-1+DNA, normalized to the average polyplex spectrum (YOYO-1+DNA spectrum obtained from Thermo Fisher Scientific). Purple line: excitation wavelength, dotted grid lines: detection window boundaries, red line: emission maximum of free YOYO-1. **E** 3D reconstruction of the respective cell with polyplexes marked as green dots,

depicting their distribution around the nucleus. A total of 77 polyplexes was identified, notably, none of which stuck to the outer cell membrane.

To monitor the uptake behavior of polyplexes and the approaching of the polyplexes to the cell surface, a time series of living cells was recorded after addition of the polyplex solution (10 min to 88 min after addition, Video S2). During the first 10 min after addition, the polyplexes could be observed settling onto the glass substrate and cells (not shown), whereas no dots were visible in the YOYO-1 channel before polyplex addition (Figure S31). Figure 5A shows the first frame of the time series. Large numbers of polyplexes are stuck to the cell membranes but only some cells have small numbers of polyplexes in the cytoplasm in the imaged plane. After 88 min, all cells in the field of view show polyplexes in the cytoplasm, though the amounts vary from below 10 to several dozens. In all cases, internalized polyplexes coincide with bright spots in the CMDR channel, indicating encapsulation in membrane vesicles and endocytosis as uptake mechanism. Illustrations emphasizing these effects are given in the SI, Figure S32-37. A discrete uptake event is documented in Figure S38. The uptake appears to happen predominantly, if not exclusively, at the tip of cell extrusions in the immediate vicinity of lamellipodia. These are also the areas of highest polyplex density and strongest polyplex agitation (Video S2), with the latter being a result of rapid filopodium and lamellipodium movement. In combination with the relative flatness of those areas (as compared to the main cell bodies), confining the polyplex movement mostly to two dimensions (*i.e.,* the imaging plane), this leads to prominent hotspots in the lamellipodial/filopodial region in a maximum intensity projection (MIP) along the time axis of the series (Figure 5B). The highly dynamic movement of filopodia leads to a hazy glow around the mostly stationary cells in this representation, showing that very few areas remain ‘unexplored’ by the cell cluster. Once taken up, we observed the polyplex containing vesicles being rapidly transported towards the cell center in most cases, as illustrated in Figure 5C. In linear approximation, the distance covered from C1 to C2 and from C2 to C3 was 5.8 µm each, corresponding to a transport velocity of

4.09 µm min^{-1}. We did not observe discrete uptake events in regions other than the above described, though it should be noted that high polyplex mobility on the cell membrane could be seen, leading to them frequently drifting into and out of focus and making it difficult to follow individual polyplexes for prolonged amounts of time. Figure 5D illustrates this drifting motion within the imaging plane. It appears to be largely passive without strong directional preferences. It can be assumed that this motion is not confined to two dimensions as individual polyplex traces in Figure 5D get darker and lighter in an unpredictable manner with some vanishing completely or suddenly appearing. This membrane drifting probably plays a role in supplying the endocytically active lamellipodia regions with polyplexes [13].

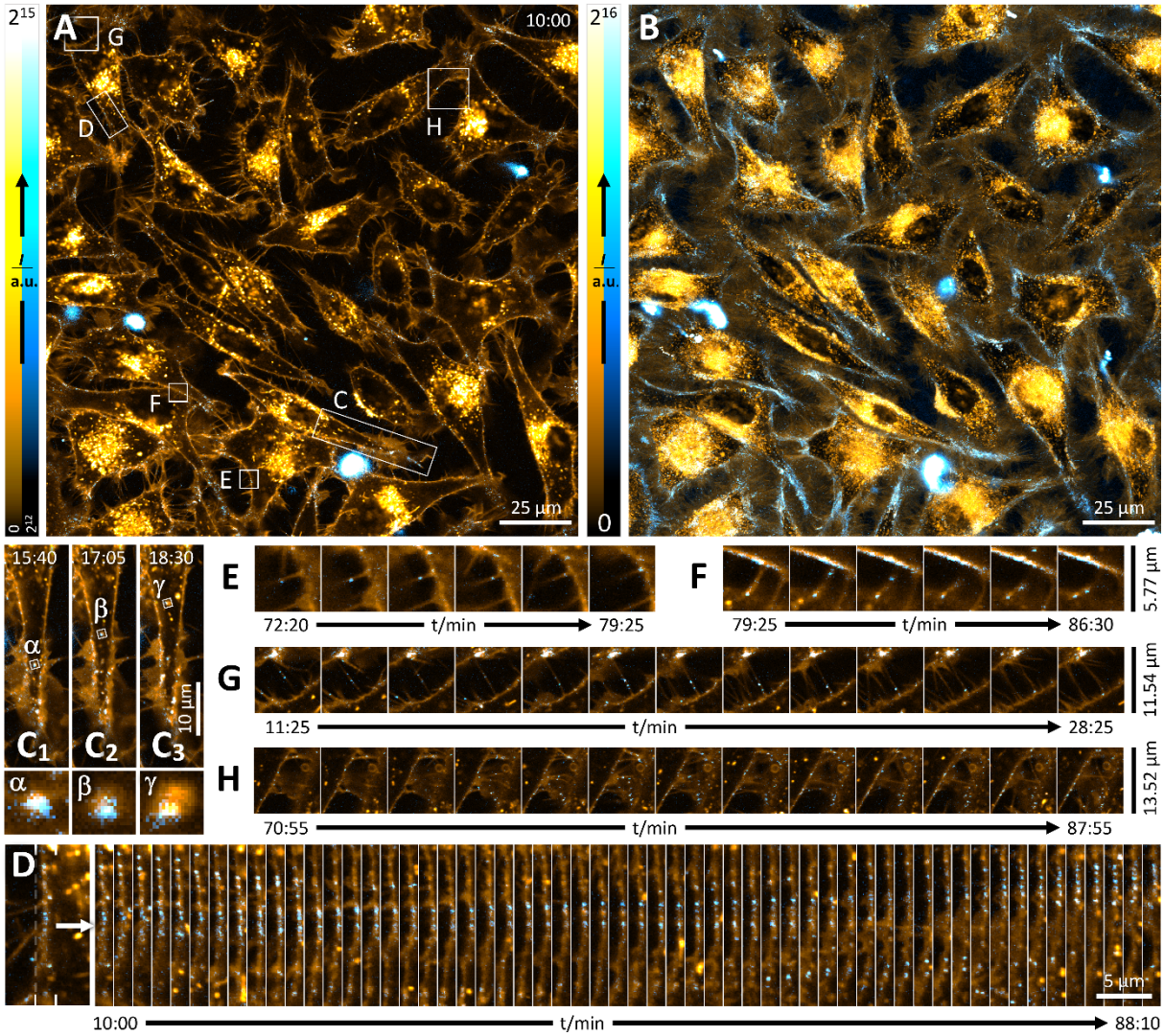

Figure 5 Time series of fluorescence images (orange: CMDR, cyan-blue: YOYO-1) of L-929 cells after addition of polypeptide polyplex (**P2**). **A** First image (t = 10 min) of the series. Cell

membranes are clearly distinguishable by CMDR staining. Each cell has a multitude of filopodia. Polyplexes have settled on the cells and stick to the membranes. **B** MIP of the series along the time axis from 10 to 88 min. **C** Series of three consecutive frames showing the rapid transport of a polyplex-containing vesicle from the lamellipodium towards the main cell body after endocytosis. Inserts α–γ have side lengths of 1.8 µm. **D** Polyplexes passively sliding along the cell membrane without strong directional preferences and with no cellular uptake occurring. All 56 frames are depicted. **E** Filopodium surfing of a single polyplex towards the membrane of the cell body. **F** A single polyplex is transferred from the membrane of one cell to that of another *via* filopodium surfing. **G** Filopodium bridges between cells mediate polyplex exchange. **H** Lamellipodium of one cell touches another cell's membrane. Large numbers of polyplexes are transported *via* the gap in a relatively short time span.

As mentioned above, an interesting observation is the mode of polyplex acquisition and initial interaction with the cells. In contrast to those polyplexes, which initially settle on the cells, others are actively transported from the vicinity towards the cells *via* filopodium surfing by a large number of filopodia, constantly exploring the cells' surroundings.[13, 70] One of the numerous examples of this effect is depicted in Figure 5E. This surfing motion appears to be independent of filopodium retraction,[71] though in many cases these effects are difficult to separate. Particularly interesting in this regard is the role of cell-bridging filopodia. In areas of close contact, stretches of the cell membrane with more than 1 bridging filopodium per 1 µm are not uncommon, often with unclear filopodium affiliation (compare also Figure S41). These bridges can be brief contacts, lasting only for a few minutes, but also remarkably long-lived with examples in the here discussed dataset lasting for almost 1 h. Polyplex transport along those bridges occurs as for non-bridging filopodia (Figure 5G). While in many cases the polyplex origin is unclear, in others, filopodia of one cell clearly detach polyplexes from another cell's membrane and subsequently acquire it (Figure 5F). A similar transfer effect can be observed where lamellipodia of one cell touch another cell's membrane (Figure 5H), though, again, the polyplex' origin remains unclear in this example. These findings (regarding the role of lamellipodia and filopodia in the initial contact of cells with particle like structures such as polyplexes, their acquisition and transport by surfing on and retraction of filopodia and cell-to-cell distribution) have been firstly shown for viruses attaching to the filopodia and surfing towards the cell surface and main body where they are taken up by the cell.[72, 73] Subsequent to

744 reaching the cell surface by help of the filopodia, the particle like structures are taken up by
745 several endocytic processes, *e.g.*, clathrin- and caveolae-mediated endocytosis and
746 macropinocytosis, ending up in the endolysosomal pathway (early endosomes), which is
747 usually desired for non-viral gene delivery systems.[74, 75] The uptake thereby often occurs in the
748 endocytically active lamellipodia regions as also observed within this study.[13] This mechanism
749 of acquisition followed by endocytic uptake can be probably attributed to the enrichment of
750 proteoglycan receptors such as syndecans on filopodia, known to facilitate interaction with
751 cationic particles such as cationic non-viral vectors.[72, 76] However, so far little is known about
752 the initial interaction and approaching of non-viral gene delivery vectors to cells and the role
753 of this mechanism in the transfection process is largely unrecognized and underappreciated, as
754 only few studies investigated this mechanism for lipoplexes and hydrophilic polyplexes.[13, 70] In
755 this study, it has now firstly been shown that this mechanism also plays a role for amphiphilic
756 polyplexes and their subsequent cellular internalization and is thus an important aspect and
757 promising approach for further optimizing the transfection efficiency of such polyplexes in
758 future studies. The proposed mechanism is shown in simplified form in Scheme 1.

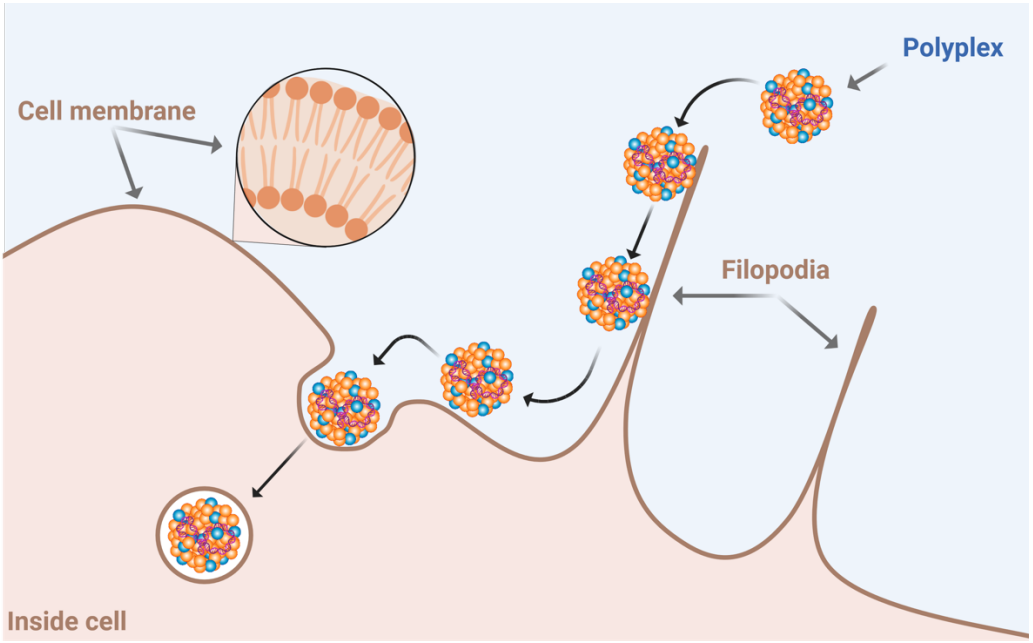

759

760 **Scheme 1** Proposed mechanism of polyplex acquisition and their transport by surfing on
761 filopodia.

Cellular Uptake Measured via Transmission Electron Microscopy. In order to further evaluate the uptake mechanism following polyplex acquisition by the lamellipodia and filopodia and the intracellular polyplex location, TEM measurements of L-929 cells incubated with **P2** N/P 5 and **P3** N/P 10 polyplexes for 1 h were conducted. It was possible to identify several cellular substructures, *e.g*., the nucleus and endolysosomal vesicles within the obtained TEM images. Further structures with high electron density were observed, which were attributed to **P2** and **P3** polyplexes that were stained with uranyl acetate.[77] In both samples, the polyplexes appear as nearly spherical nanosized structures and for **P3** N/P 10, partial agglomeration of polyplexes in the extracellular environment was observed, which is in line with the cryo-TEM measurements (Figure S 25). Both samples show location of single or multiple nanosized polyplexes in endolysosomal vesicles. These observations complement the NTA measurements of centrifuged **P2** polyplexes and the fluorescence microscopy measurements, again confirming the presence of nanosized polyplexes besides larger aggregates (Figure S24, Figure 5, Table S5). Furthermore, these results illustrate that larger aggregates are not taken up by cells within an hour, which correlates with the fluorescence microscopy measurements. Subsequent to cellular uptake, within the endolysosomal vesicles, polyplexes are often associated with the vesicle membranes and partially result in membrane deformation. These results confirm the active endocytic uptake of **P2** and **P3** polyplexes into L-929 cells as observed by fluorescence microscopy.[78, 79] However, no qualitative differences between **P2** and **P3** regarding location or membrane interaction were observed in TEM measurements following 1 h incubation.

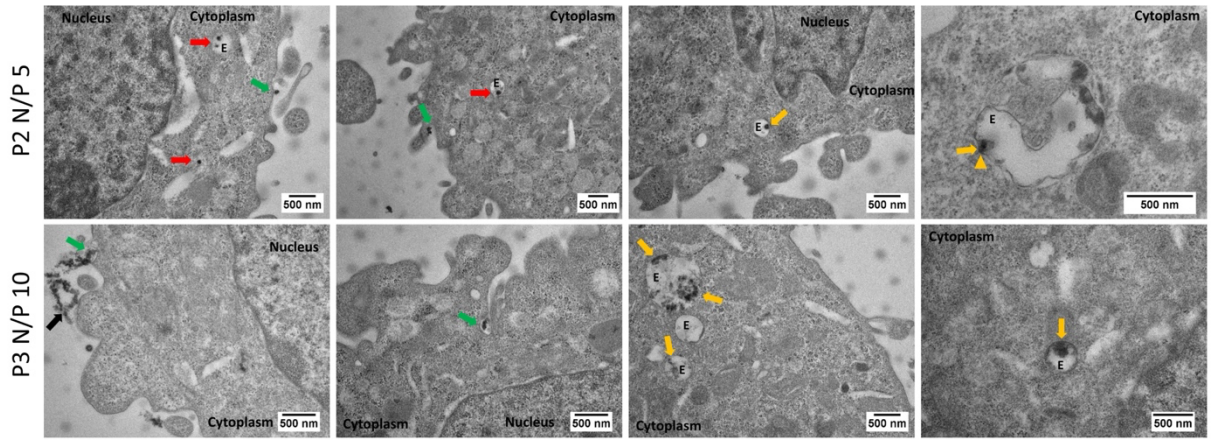

Figure 6 TEM images of L-929 cells incubated with **P2** N/P 5 and **P3** N/P 10 polyplexes for 1 h. Electron dense structures (black) were identified as polyplexes. Black arrows indicate extracellular accumulation of polyplex structures. Green arrows indicate polyplex-cell interaction or uptake events. The location of polyplexes in vesicles, *e.g.*, endosomes (E) is indicated by red arrows. Yellow arrows indicate interaction of polyplexes with vesicle membranes and the deformation of these membranes by polyplexes is indicated by yellow arrow heads.

In summary, a filopodia- and lamellipodia-based endocytic uptake mechanism was observed for both **P3** N/P 10 polyplexes and the nanosized portion of **P2** N/P 5 polyplexes. Quantitative flow cytometry measurements revealed faster and more homogeneous uptake kinetics for **P3** N/P 10 compared to **P2** N/P 5 polyplexes, but the uptake levels (percentage of cells, rMFI) after 24 h were similar (Figure 3E). Notwithstanding, the transfection efficiency is substantially higher for **P3** N/P 10 after 24 h incubation. This might be explained by higher endosomal release efficiency observed after 1 h, facilitated by higher membrane interaction of the **P3** polymer and faster polyplex uptake resulting in high endosomal polyplex concentration.[80] Nevertheless, the escape efficiency is rather low and not substantially higher than for **P1** and **P2**. This leads to the assumption that endosomal escape might take place over longer time periods, steadily releasing the polyplexes resulting in higher transfection efficiency compared to the other polypeptides.

CONCLUSION

A selected number of amphiphilic polypeptides containing different distributions of cationic AB-L-Gln (100, 84, 60, 30 and 0 mol%) and aliphatic Hex-L-Gln (0, 16, 40, 70 and 100 mol%) side chains were obtained *via* an efficient four-step synthesis. It was shown that the secondary

structure of P(AB-L-Gln-*stat*-Hex-L-Gln) can be influenced by varying the distribution of both cationic and aliphatic units.

The water-soluble polypeptides **P1**, **P2** and **P3** were evaluated for their ability to complex pDNA, showing sufficient binding and release capability. An intensive screening of the transfection performance of the polyplexes in the mouse fibroblast cell line L-929 revealed **P3** as clear outperformer over the other polypeptides and commercial LPEI. Polyplexes formed with the **P3** polypeptide comprising the highest proportion of hydrophobic HexA groups and highest amount of ordered secondary structures such as α- helical and β-sheet structures resulted in the highest percentage of EGFP expressing cells in comparison to **P1** and **P2** at similar N/P ratios and, thus, similar amount of cationic charges, while maintaining high cell viability. In-depth investigation of the interaction with erythrocyte membranes as a model system and with L-929 cells illustrated the highest membrane interaction and endosomal release levels of **P3** polyplexes. Evaluation of cellular uptake by flow cytometry revealed that **P3** polyplexes were taken up by almost all cells after 1 h, which was observed for **P2** polyplexes only after a longer incubation period. This difference was attributed to the presence of larger aggregates besides nanosized polyplexes in **P2**. Time- and z-resolved fluorescence microscopy and TEM demonstrated an active filopodia- and lamellipodia-based initial acquisition of the nanosized polyplexes present in **P2** and **P3** followed by endocytic uptake mechanisms for both polypeptides, showing no qualitative difference within the polypeptides. In both cases, cells were found to actively explore the surroundings with their filopodia and acquire the polyplexes before transporting them towards the main cell body, predominantly by filopodium surfing, possibly in combination with filopodium retraction. The polyplexes presented here exhibited high mobility on the cell surface, where they can reside for prolonged amounts of time. Polyplex uptake appears to happen in a strictly localized fashion in the very active lamellipodia regions, followed by active transport to the cell interior. In combination with higher endosomal release

efficiency, facilitated by higher membrane interaction, the faster and more homogenous polyplex uptake mediated by filopodia- and lamellipodia-based initial acquisition resulted in substantially higher transfection efficiency of the **P3** polypeptide outperforming the other polypeptides.

Taken together, these results give insight into the gene transfer process of amphiphilic polypeptides including the mechanism of initial polyplex acquisition and internalization and reveal the potential of the integration of aliphatic groups into cationic polypeptides to obtain nanosized, effective, biocompatible, and potentially biodegradable gene delivery vectors. The straightforward and versatile synthesis of polypeptides by post-polymerization functionalization provides a promising platform for further optimization and fine-tuning in terms of charge, hydrophobicity, secondary structure, and the introduction of shielding units such as PEG in order to develop highly efficient amphipathic polypeptides that are capable of overcoming the physiological barriers faced when delivering pDNA but also other cargos such as siRNA and mRNA *in vitro* and *in vivo*. Imaging techniques such as fluorescence microscopy and transmission electron microscopy help understanding the involved processes and interactions on a subcellular level and in particular allow to study the so far largely unrecognized and for amphiphilic polypeptides unstudied lamellipodia- and filopodia-based mechanism of initial interaction of the with cells. This offers the possibility for further design and optimization of tailor-made polypeptide-based vectors.

ASSOCIATED CONTENT

Supporting information

The datasets used and/or analyzed during the current study are available from the corresponding author on reasonable request. Additional material, methods, and results, including Figure S1 - S43, Tables S1 - S5, Videos S1 - S4, are collected in the Supplementary Information.

FUNDING

This work was financially supported by the Collaborative Research Center PolyTarget (SFB 1278 - projects B01, C01, Z01, project ID 316213987) funded by the German Research Foundation (DFG). TEM and cryo-TEM investigations were performed at the electron microscopy facilities of the Jena Center for Soft Matter (JCSM), which were purchased with grants from the DFG and the European funds for Regional Development (EFRE). Furthermore, the authors thank the Bundesministerium für Bildung und Forschung (BMBF, Germany, #13XP5034A PolyBioMik). The LSM8800 ELYRA PS.1 was kindly funded by the DFG.

NOTES

The authors declare that they have no competing interests. Scheme 1 was created using BioRender.

ACKNOWLEDGEMENTS

The authors thankfully acknowledge Carolin Kellner, Bärbel Beringer-Siemers, Elisabeth Preußger and Maria Stumpf for their excellent technical support and Dr. Grit Festag for maintaining the SEC facilities. Furthermore, the authors thankfully acknowledge Elisabeth Moek for support with the transfection assays and Constanze Schulz and Arnica Karuna for support with fluorescence microscopy measurements. The authors gratefully thank Prof. U. S. Schubert for providing excellent facilities and his continuous support.

REFERENCES

(1) Salas-Ambrosio, P.; Tronnet, A.; Verhaeghe, P.; Bonduelle, C. Synthetic Polypeptide Polymers as Simplified Analogues of Antimicrobial Peptides. *Biomacromolecules* **2021,** *22*, 57-75.

(2) Sang, X.; Yang, Q.; Wen, Q.; Zhang, L.; Ni, C. Preparation and Controlled Drug Release Ability of the Poly[N-Isopropylacryamide-co-Allyl Poly(Ethylene Glycol)]-b-Poly(γ-Benzyl-L-Glutamate) Polymeric Micelles. *Mater. Sci. Eng. C* **2019,** *98*, 910-917.

(3) Tesauro, D.; Accardo, A.; Diaferia, C.; Milano, V.; Guillon, J.; Ronga, L.; Rossi, F. Peptide-Based Drug-Delivery Systems in Biotechnological Applications: Recent Advances and Perspectives. *Molecules* **2019,** *24*, 351-377.

(4) Zeng, X.; Wang, L.; Liu, D.; Liu, D. Poly(L-Lysine)-Based Cylindrical Copolypeptide Brushes as Potential Drug and Gene Carriers. *Colloid Polym. Sci.* **2016,** *294*, 1909-1920.

(5) Klemm, P.; Behnke, M.; Solomun, J. I.; Bonduelle, C.; Lecommandoux, S.; Traeger, A.; Schubert, S. Self-Assembled PEGylated Amphiphilic Polypeptides for Gene Transfection. *J. Mater. Chem. B* **2021,** *9*, 8224-8236.

(6) Song, Y.; Chen, Y.; Li, P.; Dong, C.-M. Photoresponsive Polypeptide-Glycosylated Dendron Amphiphiles: UV-Triggered Polymersomes, OVA Release, and In Vitro Enhanced Uptake and Immune Response. *Biomacromolecules* **2020,** *21*, 5345-5357.

(7) Dunbar Cynthia, E.; High Katherine, A.; Joung, J. K.; Kohn Donald, B.; Ozawa, K.; Sadelain, M. Gene Therapy Comes of Age. *Science* **2018,** *359*, eaan4672.

(8) Wahane, A.; Waghmode, A.; Kapphahn, A.; Dhuri, K.; Gupta, A.; Bahal, R. Role of Lipid-Based and Polymer-Based Non-Viral Vectors in Nucleic Acid Delivery for Next-Generation Gene Therapy. *Molecules* **2020,** *25*, 2866-2888.

(9) Durymanov, M.; Reineke, J. Non-Viral Delivery of Nucleic Acids: Insight Into Mechanisms of Overcoming Intracellular Barriers. *Front. Pharmacol.* **2018,** *9*, 971.

(10) Lächelt, U.; Wagner, E. Nucleic Acid Therapeutics Using Polyplexes: A Journey of 50 Years (and Beyond). *Chem. Rev.* **2015,** *115*, 11043-11078.

(11) Bus, T.; Traeger, A.; Schubert, U. S. The Great Escape: How Cationic Polyplexes Overcome The Endosomal Barrier. *J. Mater. Chem. B* **2018,** *6*, 6904-6918.

(12) Kou, L.; Sun, J.; Zhai, Y.; He, Z. The Endocytosis and Intracellular Fate of Nanomedicines: Implication for Rational Design. *Asian J. of Pharm.* **2013,** *8*, 1-10.

(13) Ingle, N. P.; Hexum, J. K.; Reineke, T. M. Polyplexes Are Endocytosed by and Trafficked within Filopodia. *Biomacromolecules* **2020,** *21*, 1379-1392.

(14) Monsigny, M.; Roche, A.-C.; Midoux, P.; Mayer, R. Glycoconjugates as Carriers for Specific Delivery of Therapeutic Drugs and Genes. *Adv. Drug Deliv. Rev.* **1994,** *14*, 1-24.

(15) Wagner, E.; Curiel, D.; Cotten, M. Delivery of Drugs, Proteins and Genes into Cells Using Transferrin as a Ligand for Receptor-Mediated Endocytosis. *Adv. Drug Deliv. Rev.* **1994,** *14*, 113-135.

(16) Eiríksdóttir, E.; Konate, K.; Langel, Ü.; Divita, G.; Deshayes, S. Secondary Structure of Cell-Penetrating Peptides Controls Membrane Interaction and Insertion. *Biochim. Biophys. Acta* **2010,** *1798*, 1119-1128.

(17) Song, Z.; Fu, H.; Wang, R.; Pacheco, L. A.; Wang, X.; Lin, Y.; Cheng, J. Secondary Structures in Synthetic Polypeptides from N-carboxyanhydrides: Design, Modulation, Association, and Material Applications. *Chem. Soc. Rev.* **2018,** *47*, 7401-7425.

(18) Koren, E.; Torchilin, V. P. Cell-Penetrating Peptides: Breaking Through to the Other Side. *Trends Mol. Med.* **2012,** *18*, 385-393.

(19) Lee, M. W.; Han, M.; Bossa, G. V.; Snell, C.; Song, Z.; Tang, H.; Yin, L.; Cheng, J.; May, S.; Luijten, E.; Wong, G. C. L. Interactions between Membranes and "Metaphilic" Polypeptide Architectures with Diverse Side-Chain Populations. *ACS Nano* **2017,** *11*, 2858-2871.

(20) Rajpal; Mann, A.; Khanduri, R.; Naik, R. J.; Ganguli, M. Structural Rearrangements and Chemical Modifications in Known Cell Penetrating Peptide Strongly Enhance DNA Delivery Efficiency. *J. Control. Release* **2012,** *157*, 260-271.

(21) Gabrielson, N. P.; Lu, H.; Yin, L.; Li, D.; Wang, F.; Cheng, J. Reactive and Bioactive Cationic α-Helical Polypeptide Template for Nonviral Gene Delivery. *Angew. Chem Int. Ed.* **2012,** *51*, 1143-1147.

(22) Mann, A.; Thakur, G.; Shukla, V.; Ganguli, M. Peptides in DNA Delivery: Current Insights and Future Directions. *Drug Discov. Today* **2008,** *13*, 152-160.

(23) González-Henríquez, C. M.; Sarabia-Vallejos, M. A.; Rodríguez-Hernández, J. Strategies to Fabricate Polypeptide-Based Structures via Ring-Opening Polymerization of N-Carboxyanhydrides. *Polymers* **2017,** *9*, 511.

(24) Rasines Mazo, A.; Allison-Logan, S.; Karimi, F.; Chan, N. J.-A.; Qiu, W.; Duan, W.; O'Brien-Simpson, N. M.; Qiao, G. G. Ring Opening Polymerization of α-Amino Acids: Advances in Synthesis, Architecture and Applications of Polypeptides and Their Hybrids. *Chem. Soc. Rev.* **2020,** *49*, 4737-4834.

(25) Bonduelle, C.; Huang, J.; Ibarboure, E.; Heise, A.; Lecommandoux, S. Synthesis and Self-Aassembly of "Tree-Like" Amphiphilic Glycopolypeptides. *Chem. Commun.* **2012,** *48*, 8353-8355.

(26) Quadir, M. A.; Martin, M.; Hammond, P. T. Clickable Synthetic Polypeptides—Routes to New Highly Adaptive Biomaterials. *Chem. Mater.* **2014,** *26*, 461-476.

(27) Schatz, C.; Louguet, S.; Le Meins, J.-F.; Lecommandoux, S. Polysaccharide-block-polypeptide Copolymer Vesicles: Towards Synthetic Viral Capsids. *Angew. Chem. int. Ed.* **2009,** *48*, 2572-2575.

(28) Guo, J.; Huang, Y.; Jing, X.; Chen, X. Synthesis and Characterization of Functional Poly(γ-Benzyl-L-Glutamate) (PBLG) as a Hydrophobic Precursor. *Polymer* **2009,** *50*, 2847-2855.

(29) Manai, G.; Houimel, H.; Rigoulet, M.; Gillet, A.; Fazzini, P.-F.; Ibarra, A.; Balor, S.; Roblin, P.; Esvan, J.; Coppel, Y.; Chaudret, B.; Bonduelle, C.; Tricard, S. Bidimensional Lamellar Assembly by Coordination of Peptidic Homopolymers to Platinum Nanoparticles. *Nat. Commun.* **2020,** *11*, 2051-2057.

(30) Barz, M.; Duro-Castano, A.; Vicent, M. J. A Versatile Post-Polymerization Modification Method for Polyglutamic Acid: Synthesis of Orthogonal Reactive Polyglutamates and Their Use in "Click Chemistry". *Polym. Chem.* **2013,** *4*, 2989-2994.

(31) Mildner, R.; Menzel, H. Facile Synthesis of pH-Responsive Glycopolypeptides with Adjustable Sugar Density. *J. Polym. Sci. A Polym. Chem.* **2013,** *51*, 3925-3931.

(32) Krivitsky, A.; Polyak, D.; Scomparin, A.; Eliyahu, S.; Ori, A.; Avkin-Nachum, S.; Krivitsky, V.; Satchi-Fainaro, R. Structure–Function Correlation of Aminated Poly(α)glutamate as siRNA Nanocarriers. *Biomacromolecules* **2016,** *17*, 2787-2800.

(33) Niño-Pariente, A.; Armiñán, A.; Reinhard, S.; Scholz, C.; Wagner, E.; Vicent, M. J. Design of Poly-L-Glutamate-Based Complexes for pDNA Delivery. *Macromol. Biosci.* **2017,** *17*, 1700029.

(34) Callari, M.; Wong, S.; Lu, H.; Aldrich-Wright, J.; de Souza, P.; Stenzel, M. H. Drug Induced Self-Assembly of Triblock Copolymers into Polymersomes for the Synergistic Dual-Drug Delivery of Platinum Drugs and Paclitaxel. *Polym. Chem.* **2017,** *8*, 6289-6299.

(35) Singer, J.; Baker, B.; de Vries, P.; Kumar, A.; Shaffer, S.; Vawter, E.; Bolton, M.; Garzone, P. Poly-(L)-Glutamic Acid-Paclitaxel (CT-2103) [XYOTAX], a Biodegradable Polymeric Drug Conjugate: Characterization, Preclinical Pharmacology, and Preliminary Clinical Data. *Adv. Exp. Med. Biol.* **2003,** *519*, 81-109.

(36) Paclitaxel, Polyglutamate Paclitaxel, or Observation in Treating Patients With Stage III or Stage IV Ovarian Epithelial, Peritoneal Cancer, or Fallopian Tube Cancer. https://clinicaltrials.gov/ct2/show/NCT00108745?term=Poly-%28L%29-glutamic+acid-paclitaxel&draw=2&rank=2#wrapper (October 18, 2021),

(37) Tang, H.; Yin, L.; Kim, K. H.; Cheng, J. Helical Poly(Arginine) Mimics with Superior Cell-Penetrating and Molecular Transporting Properties. *Chem. Sci.* **2013,** *4*, 3839-3844.

(38) Gabrielson, N. P.; Lu, H.; Yin, L.; Li, D.; Wang, F.; Cheng, J. Reactive and Bioactive Cationic α-Helical Polypeptide Template for Nonviral Gene Delivery. **2012,** *51*, 1143-1147.

(39) Ge, C.; Yang, J.; Duan, S.; Liu, Y.; Meng, F.; Yin, L. Fluorinated α-Helical Polypeptides Synchronize Mucus Permeation and Cell Penetration toward Highly Efficient Pulmonary siRNA Delivery against Acute Lung Injury. *Nano Letters* **2020,** *20*, 1738-1746.

(40) Liu, B.; Zhang, Q.; Zhou, F.; Ren, L.; Zhao, Y.; Yuan, X. Enhancing Membrane-Disruptive Activity via Hydrophobic Phenylalanine and Lysine Tethered to Poly(Aspartic Acid). *ACS Appl. Mater. Interfaces* **2019,** *11*, 14538-14547.

(41) Yu, Z.; Zhang, Z.; Yan, J.; Zhao, Z.; Ge, C.; Song, Z.; Yin, L.; Tang, H. Guanidine-Rich Helical Polypeptides Bearing Hydrophobic Amino Acid Pendants for Efficient Gene Delivery. *Biomater. Sci.* **2021,** *9*, 2670-2678.

(42) Conejos-Sánchez, I.; Duro-Castano, A.; Birke, A.; Barz, M.; Vicent, M. J. A Controlled and Versatile NCA Polymerization Method for the Synthesis of Polypeptides. *Polym. Chem.* **2013,** *4*, 3182-3186.

(43) Schneider, C. A.; Rasband, W. S.; Eliceiri, K. W. NIH Image to ImageJ: 25 Years of Image Analysis. *Nat. methods* **2012,** *9*, 671-675.

(44) Richter, F.; Mapfumo, P.; Martin, L.; Solomun, J. I.; Hausig, F.; Frietsch, J. J.; Ernst, T.; Hoeppener, S.; Brendel, J. C.; Traeger, A. Improved Gene Delivery to K-562 Leukemia Cells by Lipoic Acid Modified Block Copolymer Micelles. *J. Nanobiotechnology* **2021,** *19*, 70-84.

(45) Richter, F.; Leer, K.; Martin, L.; Mapfumo, P.; Solomun, J. I.; Kuchenbrod, M. T.; Hoeppener, S.; Brendel, J. C.; Traeger, A. The Impact of Anionic Polymers on Gene Delivery: How Composition and Assembly Help Evading the Toxicity-Efficiency Dilemma. *J. Nanobiotechnology* **2021,** *19*, 292-306.

(46) Schindelin, J.; Arganda-Carreras, I.; Frise, E.; Kaynig, V.; Longair, M.; Pietzsch, T.; Preibisch, S.; Rueden, C.; Saalfeld, S.; Schmid, B.; Tinevez, J.-Y.; White, D. J.; Hartenstein, V.; Eliceiri, K.; Tomancak, P.; Cardona, A. Fiji: An Open-Source Platform for Biological-Image Analysis. *Nat. methods* **2012,** *9*, 676-682.

(47) Aescht, E.; Büchl-Zimmermann, S.; Burmester, A.; Dänhardt-Pfeiffer, S.; Desel, C.; Hamers, C.; Jach, G.; Kässens, M.; Makovitzky, J.; Mulisch, M.; Nixdorf-Bergweiler, B.; Pütz, D.; Riedelsheimer, B.; Boom, F.; Wegerhoff, R.; Welsch, U., *Romeis - Mikroskopische Technik*. 18 ed.; Springer-Verlag: Heidelberg, 2010.

(48) Bonduelle, C. Secondary Structures of Synthetic Polypeptide Polymers. *Polym. Chem.* **2018,** *9*, 1517-1529.

(49) Huesmann, D.; Birke, A.; Klinker, K.; Türk, S.; Räder, H. J.; Barz, M. Revisiting Secondary Structures in NCA Polymerization: Influences on the Analysis of Protected Polylysines. *Macromolecules* **2014,** *47*, 928-936.

(50) Miyazawa, T.; Blout, E. R. The Infrared Spectra of Polypeptides in Various Conformations: Amide I and II Bands. *J. Am. Chem. Soc.* **1961,** *83*, 712-719.

(51) Bonduelle, C.; Makni, F.; Severac, L.; Piedra-Arroni, E.; Serpentini, C.-L.; Lecommandoux, S.; Pratviel, G. Smart Metallopoly(L-Glutamic Acid) Polymers: Reversible Helix-to-Coil Transition at Neutral pH. *RSC Adv.* **2016,** *6*, 84694-84697.

(52) Eltoukhy, A. A.; Chen, D.; Alabi, C. A.; Langer, R.; Anderson, D. G. Degradable Terpolymers with Alkyl Side Chains Demonstrate Enhanced Gene Delivery Potency and Nanoparticle Stability. *Adv. Mater.* **2013,** *25*, 1487-1493.

(53) Nelson, C. E.; Kintzing, J. R.; Hanna, A.; Shannon, J. M.; Gupta, M. K.; Duvall, C. L. Balancing Cationic and Hydrophobic Content of PEGylated siRNA Polyplexes Enhances Endosome Escape, Stability, Blood Circulation Time, and Bioactivity In Vivo. *ACS Nano* **2013,** *7*, 8870-8880.

(54) Rémy-Kristensen, A.; Clamme, J.-P.; Vuilleumier, C.; Kuhry, J.-G.; Mély, Y. Role of endocytosis in the transfection of L929 fibroblasts by polyethylenimine/DNA complexes. *Biochim. Biophys. Acta Biomembr.* **2001,** *1514*, 21-32.

(55) Hertz, D.; Leiske, M. N.; Wloka, T.; Traeger, A.; Hartlieb, M.; Kessels, M. M.; Schubert, S.; Qualmann, B.; Schubert, U. S. Comparison of random and gradient amino functionalized poly(2-oxazoline)s: Can the transfection efficiency be tuned by the macromolecular structure? *J. Polym. Sci. A Polym. Chem.* **2018,** *56*, 1210-1224.

(56) Monnery, B. D.; Wright, M.; Cavill, R.; Hoogenboom, R.; Shaunak, S.; Steinke, J. H. G.; Thanou, M. Cytotoxicity of Polycations: Relationship of Molecular Weight and the Hydrolytic Theory of the Mechanism of Toxicity. *Int. J. Pharm.* **2017,** *521*, 249-258.

(57) Liu, Z.; Zhang, Z.; Zhou, C.; Jiao, Y. Hydrophobic Modifications of Cationic polymers for Gene Delivery. *Prog. Polym. Sci.* **2010,** *35*, 1144-1162.

(58) Zhang, R.; Zheng, N.; Song, Z.; Yin, L.; Cheng, J. The effect of side-chain functionality and hydrophobicity on the gene delivery capabilities of cationic helical polypeptides. *Biomaterials* **2014,** *35*, 3443-3454.

(59) Fang, H.; Guo, Z.; Lin, L.; Chen, J.; Sun, P.; Wu, J.; Xu, C.; Tian, H.; Chen, X. Molecular Strings Significantly Improved the Gene Transfection Efficiency of Polycations. *J. Am. Chem. Soc.* **2018,** *140*, 11992-12000.

(60) Huotari, J.; Helenius, A. Endosome Maturation. *EMBO J.* **2011,** *30*, 3481-3500.

(61) Incani, V.; Lavasanifar, A.; Uludağ, H. Lipid and Hydrophobic Modification of Cationic Carriers on Route to Superior Gene Vectors. *Soft Matter* **2010,** *6*, 2124-2138.

(62) Rejman, J.; Oberle, V.; Zuhorn, I. S.; Hoekstra, D. Size-Dependent Internalization of Particles via The Pathways of Clathrin- and Caveolae-Mediated Endocytosis. *Biochem. J.* **2004,** *377*, 159-169.

(63) Shang, L.; Nienhaus, K.; Nienhaus, G. U. Engineered Nanoparticles Interacting with Cells: Size Matters. *J. Nanobiotechnology* **2014,** *12*, 5-15.

(64) Tan, Z.; Jiang, Y.; Zhang, W.; Karls, L.; Lodge, T. P.; Reineke, T. M. Polycation Architecture and Assembly Direct Successful Gene Delivery: Micelleplexes Outperform Polyplexes via Optimal DNA Packaging. *J. Am. Chem. Soc.* **2019,** *141*, 15804-15817.

(65) González-Domínguez, I.; Puente-Massaguer, E.; Lavado-García, J.; Cervera, L.; Gòdia, F. Micrometric DNA/PEI polyplexes correlate with higher transient gene expression yields in HEK 293 cells. *N. Biotechnol.* **2022,** *68*, 87-96.

(66) Solomun, J. I.; Cinar, G.; Mapfumo, P.; Richter, F.; Moek, E.; Hausig, F.; Martin, L.; Hoeppener, S.; Nischang, I.; Traeger, A. Solely Aqueous Formulation of Hydrophobic Cationic Polymers for Efficient Gene Delivery. *Int. J. Pharm.* **2021,** *593*, 120080.

(67) Fröhlich, E. The role of surface charge in cellular uptake and cytotoxicity of medical nanoparticles. *Int. J. Nanomedicine* **2012,** *7*, 5577-91.

(68) Chen, J.; Wang, K.; Wu, J.; Tian, H.; Chen, X. Polycations for Gene Delivery: Dilemmas and Solutions. *Bioconjugate Chem.* **2019,** *30*, 338-349.

(69) Thermo Fisher Scientific, Fluorescence SpectraViewer YOYO-1. https://www.thermofisher.com/order/fluorescence-spectraviewer?SID=srch-svtool&UID=SVgfnDNA_2#!/ (October 4, 2021),

(70) Rehman, Z. u.; Sjollema, K. A.; Kuipers, J.; Hoekstra, D.; Zuhorn, I. S. Nonviral Gene Delivery Vectors Use Syndecan-Dependent Transport Mechanisms in Filopodia To Reach the Cell Surface. *ACS Nano* **2012,** *6*, 7521-7532.

(71) Kohler, F.; Rohrbach, A. Surfing along Filopodia: A Particle Transport Revealed by Molecular-Scale Fluctuation Analyses. *Biophys. J.* **2015,** *108*, 2114-2125.

(72) Rehman, Z.; Zuhorn, I. S.; Hoekstra, D. How cationic lipids transfer nucleic acids into cells and across cellular membranes: recent advances. *J. Control. Release* **2013,** *166*, 46-56.

(73) Lehmann, M. J.; Sherer, N. M.; Marks, C. B.; Pypaert, M.; Mothes, W. Actin- and myosin-driven movement of viruses along filopodia precedes their entry into cells. *J. Cell Biol.* **2005,** *170*, 317-325.

(74) Rejman, J.; Conese, M.; Hoekstra, D. Gene transfer by means of lipo- and polyplexes: role of clathrin and caveolae-mediated endocytosis. *J. Liposome Res.* **2006,** *16*, 237-47.

(75) Mayor, S.; Pagano, R. E. Pathways of clathrin-independent endocytosis. *Nat. Rev. Mol. Cell Biol.* **2007,** *8*, 603-612.

(76) ur Rehman, Z.; Sjollema, K. A.; Kuipers, J.; Hoekstra, D.; Zuhorn, I. S. Nonviral gene delivery vectors use syndecan-dependent transport mechanisms in filopodia to reach the cell surface. *ACS Nano* **2012,** *6*, 7521-7532.

(77) Reifarth, M.; Hoeppener, S.; Schubert, U. S. Uptake and Intracellular Fate of Engineered Nanoparticles in Mammalian Cells: Capabilities and Limitations of Transmission Electron Microscopy—Polymer-Based Nanoparticles. *Adv. Mater.* **2018,** *30*, 1703704.

(78) Gilleron, J.; Querbes, W.; Zeigerer, A.; Borodovsky, A.; Marsico, G.; Schubert, U.; Manygoats, K.; Seifert, S.; Andree, C.; Stöter, M.; Epstein-Barash, H.; Zhang, L.; Koteliansky, V.; Fitzgerald, K.; Fava, E.; Bickle, M.; Kalaidzidis, Y.; Akinc, A.; Maier, M.; Zerial, M. Image-Based Analysis of Lipid Nanoparticle–Mediated siRNA Delivery, Intracellular Trafficking and Endosomal Escape. *Nat. Biotechnol.* **2013,** *31*, 638-646.

(79) Doherty, G. J.; McMahon, H. T. Mechanisms of Endocytosis. *Annu. Rev. Biochem.* **2009,** *78*, 857-902.

(80) Smith, S. A.; Selby, L. I.; Johnston, A. P. R.; Such, G. K. The Endosomal Escape of Nanoparticles: Toward More Efficient Cellular Delivery. *Bioconjugate Chem.* **2019,** *30*, 263-272.